Aerospace **2015**, *2*, 279-311; doi:10.3390/aerospace2020279

OPEN ACCESS

aerospace

ISSN 2226-4310

www.mdpi.com/journal/aerospace

Article

Interaction between Crosswind and Aviation-Fuel Fire Engulfing a Full-Scale Composite-Type Aircraft: A Numerical Study

Hui Ying Wang * and Guo Da Wang

Institut P', Fluides–Thermique–Combustion, CNRS, ENSMA, Université de Poitiers, BP 40109, 86961 Futuroscope Chasseneuil Cedex, France; E-Mail: greatice3@163.com

* Author to whom correspondence should be addressed; E-Mail: wang@ensma.fr; Tel.: +33-5-4949-8295.

Academic Editor: Yang Zhang

Received: 3 April 2015 / Accepted: 21 May 2015 / Published: 28 May 2015

Abstract: This numerical study focuses on the fire phenomenology associated with the presence of a composite-type aircraft immersed, at one particular location and orientation, within a large aviation-fuel fire in a moving fluid medium. An extension of the eddy dissipation concept is incorporated, allowing one to investigate the roles of the wind speed and its direction on the fire growth, heat flux distribution and smoke products, such as carbon monoxide and soot. The predicted flame shape compares well with the measurements for an intermediate-scale fire. The outcome of the study is interesting, and the interaction model between turbulence and combustion is indeed adequate. The prediction indicates that interaction between the large object and fire environment combined with the influence of wind conditions dramatically affects the continuous flame shape. The increase of the wind speed results in an alteration of the distribution of the incident heat fluxes to the engulfed fuselage skin for a case where the fire and fuselage are of comparable size. The highest heat flux occurs on the windward side of the fuselage for the low and medium winds, but on the leeward side of the fuselage for the high wind. The peak in heat flux to the medium or high wind is almost equal in magnitude, but about a factor four increase of that to the low wind.

Keywords: pool fire models; crosswind; flame shape; toxic product; heat flux

1. Introduction

Large fully-turbulent fires, which result as a consequence of an aircraft accident due to engine failure, pose a severe hazard to the occupants and cargo [1]. Aviation liquid fuel is volatilized to form a cloud of combustible mixture, with subsequent gas-phase ignition and establishment of a vapor cloud fire. Furthermore, regarding the new generation of aircraft, the substitution of the aluminum-type fuselage by flammable composite material may induce large fuel release, leading to the development of a fireball. Under an external heat flux, the multilayer fuselage, including skin, thin thermo-acoustic insulation material, air layer and cabin wall, can be considered as a barrier to the fire penetration into the cabin. The burn-through time of a composite fuselage depends on the material composition of resin/carbon fibers, thickness, burning flammability, physical properties, *etc.* During a post-crash fire, burn-through of the composite fuselage should not occur within 3 min. Knowledge of the time and transition from ignition to flame spread inside cabin is of interest to guide the evacuation strategy. It is well known that reduced-scale tests do not necessarily reflect the behavior of a material in real aircraft fire situations due to the large contribution by radiation associated with soot formation. The occurrence of large fires that engulf an aircraft is numerically studied to simulate fuel spill fires adjacent to the engine. The availability of such a simulation can provide cost-effective alternatives by reducing the number of large-scale tests necessary to develop fire protection requirements or standards.

Intensive research has been carried over decades on pool fires in crossflow [2,3], though only a small proportion of the work has looked specifically at large-scale pool fires [4–6]. Large pool fires also imply poor entrainment, therefore enhanced soot production. Interaction between a flame and a crossflow was described by Lavid *et al*. [2] in terms of the ratio between buoyant and inertia forces in assessing if the flame is controlled by a natural or forced convection. Putman [3] investigated the behavior of small fires, indicating that an increase of the longitudinal ventilation rate enhanced the flame length. From tests of full-scale wind-aided fires [7], reduction in the flame length with an increase of wind speed was found. The study of Russel [8] demonstrated the alteration of the flow field and the related influence on the fire physics when a small cylinder, as compared to the fire, is fully engulfed by the flames. There have been studies [9,10] that predict the radiant heat transfer to a large horizontal cylinder engulfed in luminous flames. The analysis of Gregory [9] showed a maximum heat flux on the bottom of the cylinder skin and minimum on the top. The Birk correlation [10] predicts that the highest heat fluxes are at the top, and the values decrease along the periphery to the underside of the cylinder. The occurrence of large fires that engulf objects was experimentally and numerically studied by Gritzo [11]. Tests were conducted by Keltner [12] to simulate fuel spill fires that might occur under the wing of a transport aircraft. A considerable effort has been made by Suo-Anttila [5,6] in conducting a full-scale measurement of the temperature and heat flux distributions with the presence of a fuselage-sized cylindrical object engulfed in a large aviation fuel fire subjected to various winds. Large-scale (>10 m) liquid hydrocarbon pool fires are difficult to analyze experimentally because of the sheer scale of the fire. The computation effort of a large pool fire with a diameter of 20 m in crossflow [4] was performed, which was essential to demonstrate that Computational Fluid Dynamics (CFD) was able to assess the complex geometry or physics. Although large eddy simulation (LES) modelling appears as the most promising technique, currently there are still many limitations to its precise application to large-scale fires due to uncertainties introduced by a large grid size, which is primarily a problem of computational

economy, and other idealizations inherent in the model. Carbon monoxide, a smoke component, which is the yield of incomplete combustion, augments the overall toxicity of these products to a great extent. A high number of fatalities is due to the toxicity of smoke particulates and gases from the fire. The problem of carbon monoxide and soot productions in fires has been largely studied, and important outcomes are described by Gottuk [13,14]. It also underlies Orloff's success [15] in correlating the concentration of CO in terms of the mixture fraction. Presently, analysis of these toxic products is primarily limited to characterization of the fire in the absence of other influencing factors, such as wind condition and engulfed objects.

This work has focused on an analysis of flame spread and burning over the composite material surface of aircraft exposed to a post-crash fire in air crossflow on a scale where both radiation and buoyancy are significant. A fire model's treatment of soot formation has a profound influence on reliable predictions of mass burning of condensed fuels, flame spread, fire growth and thermal resistance of aircraft structure elements through thermal radiation. This approach to the field modelling of fire spread over condensed fuel surface includes the material properties, heat transfer to the fuel, chemical kinetics, soot and turbulence effects. An advanced fire physics model, which is the subject of the current work, requires state-of-the-art submodels (combustion, multidimensional participating radiation, soot formation, heat transfer, liquid fuel vaporization, *etc*.), which are coupled with the flow field governing momentum solution. In the Fire Dynamics Simulator (FDS5) code, all species of interest, including soot and CO productions, are derived from the fraction of the fuel mass that is converted into CO and soot, in addition to a radiative loss fraction. All of these parameters can be specified for well-ventilated fires for adjusting the species and flame temperature, but not for large-scale under-ventilated fires. The objectives of this work are to incorporate a two-step reaction model and smoke point concept within FDS5 [16] for examining the dominant hazards, such as fire growth, temperature, heat flux and smoke products, under a variety of wind conditions. Currently, the eddy dissipation concept (EDC) combustion model is also introduced in the version of FDS6; however, the soot model is not available, and the predicted heat flux is rather sensitive to the radiative loss fraction. Large computer times are required to run these advanced models, particularly for a full-scale, three-dimensional fire. The numerical model is verified by comparing the computed temperature and heat flux fields against the measurements [15,17,18] from intermediate fires. We have attempted to provide an entirely tractable solution for engineering calculations, such as aircraft fires. This makes CFD calculations of flame radiation in non-premixed flames of an arbitrary hydrocarbon fuel feasible, thereby retaining simplicity and minimizing computational expense.

2. Physical Modelling

This section outlines the physic–mathematical models invoked for the computations. The basis of the analysis is the conservation equations of mass, momentum, energy and species, a set of three-dimensional elliptic, time-dependent Navier–Stokes equations [16]. The finite-difference technique is used to discretize the mathematical representation of the reacting flow phenomena of interest here and can be found elsewhere [16].

2.1. Subgrid Kinetic Energy

In most fires, LES allows one to capture directly the primary momentum transport of turbulent non-premixed flame, which is sustained by large-scale energy-containing eddies [19] related to a typical geometry characteristic of a pool fire. The sub-grid scale (SGS) kinetic energy represents the unresolved turbulent energy and needs to be modelled. The subgrid kinetic energy, k, is solved by a transport equation, and its basic form was inspired by the work of Menon [20].

$$\frac{\partial \rho k}{\partial t} + \frac{\partial (\rho u_i k)}{\partial x_j} = \frac{\partial}{\partial x_j}\left(\mu_t \frac{\partial k}{\partial x_j}\right) - \tau_{ij,\,SGS}\frac{\partial u_i}{\partial x_j} - \rho\varepsilon \tag{1}$$

Here, μ_t is the eddy viscosity from the analysis of Smagorinsky [16]. The terms on the right side of equation represent, respectively, the transport, the production and the dissipation of subgrid kinetic energy. The production terms are determined from the shear stresses, τ_{ij}, SGS, which are evaluated from the resolved dynamic field.

The dissipation rate ε, which is rarely computed explicitly in LES, is formulated from the characteristic grid size, Δ, and the SGS kinetic energy, k.

$$\varepsilon = c_\varepsilon \frac{k^{3/2}}{\Delta} \text{ with } c_\varepsilon = 0.7 \tag{2}$$

2.2. Combustion via Two Chemical Reaction Steps

The combustion processes are governed by the convection-diffusion equations for the mass fraction, Y_i, of the six major chemical species, such as C_mH_n, O_2, CO, CO_2, H_2O and N_2. The mixing-controlled combustion via two chemical reaction steps for CO formation is assumed.

$$\mathrm{C}_m\mathrm{H}_n + \left(\frac{m}{2} + \frac{n}{4}\right)\mathrm{O}_2 \rightarrow m\mathrm{CO} + \frac{n}{2}\mathrm{H}_2\mathrm{O} \tag{3}$$

$$\mathrm{CO} + \frac{1}{2}\mathrm{O}_2 \rightarrow \mathrm{CO}_2 \tag{4}$$

In the turbulent regime, the turbulence is very intense compared to the chemical time, allowing a perfect mixing of fuel and oxidant before the reaction occurs. In terms of limiting the concentration of fuel or oxygen, this regime is referred to as a perfectly stirred reactor as in the EDC combustion model [21].

$$\dot{\omega}_\iota = \frac{d\rho Y_i}{dt} = -\rho\tau_{mix}\min(Y_i, \frac{Y_{O_2}}{v_{g,i}}) \cdot H_{eav}(Y_{O_2} - Y_{O_2,Lim}) \tag{5}$$

where $v_{g,i}$ denotes the stoichiometric coefficient and Y_i the fuel/CO mass fractions. The source term is multiplied by $H_{\mathrm{eav}}(Y_{\mathrm{O2}} - Y_{\mathrm{O2,Lim}})$, where H_{eav} is the Heaviside unit step function, which is zero when its argument is negative ($Y_{\mathrm{O2}} < Y_{\mathrm{O2,Lim}}$, *i.e.*, $Y_{\mathrm{O2}} \in$ no burn range) and one when it is positive ($Y_{\mathrm{O2}} > Y_{\mathrm{O2,Lim}}$ *i.e.*, $Y_{\mathrm{O2}} \in$ burn range). The oxygen limit, $Y_{\mathrm{O2,Lim}}$, for combustion is a function of the local gas temperature [16], given as:

$$Y_{O2,Lim} = \frac{C_p(T_f - T)}{\Delta H_{O_2}} \tag{6}$$

where C_p is the mixture specific heat, T_f the flame temperature and ΔH_{O2} the heat of combustion for burning 1 kg of oxygen. This simple flame extinction model allows the simulation of fire growth and smoke stratification in a progressively vitiated environment. The eddy dissipation concept (EDC) assumes that the chemical reaction in a turbulent flow takes place where reactants and hot products are molecularly mixed.

Regarding the chemical reaction time, one need only consider the first step as being instantaneous, independent of the temperature level. The second step is much slower than the first one, and the oxidation rate of CO is also evaluated from an Arrhenius expression [22],

$$\dot{\omega}_{\mathrm{CO,ARR}} = -A\exp(-\frac{E}{RT})[\mathrm{CO}][\mathrm{H_2O}]^{0.5}[\mathrm{O_2}]^{0.25} \tag{7}$$

This overall rate expression (7) for the carbon monoxide-oxygen reaction is established from a turbulent flow reactor in the presence of water. The local reaction rate of CO is crudely accounted for with the slower rate of the mixing rate (Equation (5)) and the Arrhenius one (Equation (7)). This combustion model in non-premixed flames is made tractable by their inherent simplicity. The heat release rate is determined from the consumption rate of the two combustibles of CO and C_mH_n.

In non-premixed flame, the locations of the flame front and peak temperature are controlled by the stoichiometry of the reactants rather than complex Kolmogorov time scale that governs premixed flames. Overall, heat release rates are controlled by the diffusion of reactants to a thin flame sheet separating the fuel from the oxidant. Simplicity is achieved by the recognition that the reaction in a pool-like fire is controlled by the diffusion of oxygen into the reactive zone. The key time scale, τ_{mix}, is supposed to relate approximately to the dissipation rate in SGS as below:

$$\tau_{mix} \approx C_{EDC}\frac{\varepsilon}{k} \tag{8}$$

A dynamic modelling method [23] is applied to obtain an appropriate value of the coefficient C_{EDC}, allowing one to take into account the mass transfer rate between the fine structures and the bulk of the fluid.

$$C_{EDC} = 23.6\left(\frac{\nu\varepsilon}{k^2}\right)^{1/4}\frac{\chi}{1-\chi\gamma} \tag{9}$$

where γ is the fraction of the fluid contained within the fine structures and v the kinematic viscosity.

$$\gamma = 9.7\left(\frac{\nu\varepsilon}{k^2}\right)^{3/4} \tag{10}$$

Here, χ is a factor between zero and one to express the fraction of the fine structures, which can react as a function of the mixture fraction Z.

$$\chi = \frac{Z}{Z_{st}} \; if \; 0 \le Z < Z_{st} \text{ and } \chi = \frac{1-Z}{1-Z_{st}} \qquad if \; Z_{st} \le Z \le 1 \tag{11}$$

Here, Z_{st} is the stoichiometric mixture fraction.

2.3. Radiative Heat Transfer

For a heavily sooting flame, such as fire, radiation is a crucial aspect of combustion and can dominate other modes of heat transfer. A radiative transfer equation (RTE) is solved by using a discrete expression adapted to a finite volume method [16].

$$\vec{\nabla}.\vec{\Omega}I + \kappa I = \kappa\frac{\sigma T^4}{\pi} \tag{12}$$

As the radiation spectrum of soot is continuous, it is assumed that the mixture of soot and gas behaves as a gray medium with a mean absorption coefficient, κ, used in RTE. For simplicity, six bands are selected to give an accurate representation of the most important radiation bands of CO_2 and H_2O. For the calculation of the gray or band-mean gas absorption coefficient, κ_g, a narrow-band model (RadCal) has been implemented in FDS5 [16]. Soot is the dominant influence on the absorption coefficient in large fires, and it has been established that the majority of the radiation in a fire plume (>90%) is derived from the visible part of the flame, where soot particles are radiating heat [24]. The effect of soot concentration on radiation is included by adding the radiation coefficient of soot, κ_s, into that of gas:

$$\kappa = \kappa_s + \kappa_g \tag{13}$$

where the soot absorption coefficient is calculated as a function of the temperature, T, and soot mass fraction, Y_s [25]:

$$\kappa_s = 1225T\frac{\rho Y_s}{\rho_{soot}} \tag{14}$$

2.4. Soot Formation and Its Oxidation

Soot production in fire plumes is a highly complex subject due to the spatially-varying formation and oxidation processes, the influence of turbulent fluctuations and strong temperature and fuel-dependent effects. Nevertheless, a number of researchers [25,26] have had some success in identifying factors that allow simplified analysis. The current model uses the classic principle of smoke point to relate soot production to material properties. A fuel's smoke point (SP) is the maximum height of its laminar flame burning in air at which soot is not released from the flame tip.

A global soot formation model is incorporated into a turbulent flow calculation in a convection-diffusion equation for the soot mass fraction.

$$\frac{\partial \rho Y_s}{\partial t} + \frac{\partial(\rho u_i Y_s)}{\partial x_j} - \frac{\partial}{\partial x_j}\left(\frac{\mu_t}{Sc_t}\frac{\partial Y_s}{\partial x_j}\right) = \dot{\omega}_s \tag{15}$$

The soot production rate is written as:

$$\dot{\omega}_s = \begin{cases} \dot{\omega}_f - \dot{\omega}_O & (Z \in [Z_{so}, Z_c]) \\ -\dot{\omega}_O & (Z \in [0, Z_{so}]) \end{cases} \tag{16}$$

Two mixture fraction limits delimit the soot formation and oxidation regions. The incipient mixture fraction is $Z_c = 0.15$, and the mixture fraction threshold where soot oxidation starts is $Z_{so} = 0.1$. Soot formation is assumed to be controlled by second-order homogeneous gaseous reaction processes and,

thus, is expressed as a function of the mixture fraction, Z, and gas temperature, T, both affected by a pulsing behavior in turbulent flames.

$$\dot{\omega}_f = A_f \rho^2 (\frac{Z - Z_{st}}{1 - Z_{st}}) T^{\gamma} \exp(-\frac{T_\alpha}{T}) \tag{17}$$

Here, the temperature exponent γ = 2.25 and activation temperature T_α = 2000 K are assigned. The parameter for differences in sooting behavior of different fuels is the pre-exponential factor, A_f, which is reversely proportional to the smoke point height, which has been measured for many fuels [25].

Turbulent mixing and fluctuations reduce the peak of soot concentrations as compared to that in laminar diffusion flames [15]. The soot oxidation in Equation (16) is assumed to proceed through a single reaction step,

$$\mathrm{C}_s + \mathrm{O}_2 \rightarrow \mathrm{CO}_2 \tag{18}$$

In turbulent flame, there remain some approximations due to turbulence interactions. By assuming that the mixing time is the limiting mechanism, the specific rate of soot oxidation in the turbulent reacting region is expressed by an EDC approach:

$$\dot{\omega}_o = \rho \tau_{mix} \min(Y_s, \frac{Y_{O_2}}{v_s}) \tag{19}$$

where v_s denotes the stoichiometric coefficient for burning 1 kg of soot. This approximation contains no chemically kinetic mechanism to suppress homogeneous soot formation by O_2. Outside the turbulent reacting region, the soot oxidation rate becomes much slower and is assumed to be controlled by an Arrhenius reaction processes [27]:

$$\dot{\omega}_o = A_O X_{O_2} T^{1/2} \exp(-\frac{E}{RT}) \tag{20}$$

Although the smoke point concept is incapable of accurately reproducing soot surface growth, it should be capable of capturing global trends for use in engineering calculations of radiation and visibility in fires.

2.5. Phase Coupling Conditions

The condensed fuel is assumed to be thermally-thick; a one-dimensional heat conduction equation for the material temperature is solved. The surface temperature, T_s, is affected by gains and losses with the heat balance across the interface:

$$-k_l \frac{dT_s}{dn} = \dot{q}''_{conv} + \dot{q}''_{rad} - \dot{m}''_s L_v \tag{21}$$

Here, k_l is the condensed fuel thermal conductivity and L_v the fuel latent heat. Flame radiation flux, $\dot{q}''_{rad}$, is computed from a discrete representation of the radiative intensity Equation (11). The Couette flow is assumed to prevail near the wall surface, and the convective heat feedback is calculated from a wall function [28] far away from the wall for viscous effects to be negligible, that is at $y^+ \geq 11$.

$$\dot{q}''_{conv} = \frac{(T_g - T_s) \rho C_p C_\mu^{1/4} k^{1/2}}{Pr[\frac{1}{\kappa} \ln(E y^+) + P]} \tag{22}$$

Here, C_μ and E are the constants in the logarithmic law of the wall, κ is the von Karman constant, Pr the Prandtl number, C_p the gas specific heat and P an empirical function defined by Djilali [28].

The vaporization rate of condensed fuel can be derived from the combination of the species and energy equations [29] and expressed as follows:

$$\dot{m}'' = \left(h_{m,conv} + h_{m,ray}\right) \ln(B + 1) \tag{23}$$

Here, the convective ($h_{m,conv}$) and radiative ($h_{m,ray}$) mass transfer coefficients are defined, respectively, as,

$$h_{m,\,conv} = \frac{\rho\alpha}{l} Nu \tag{24}$$

$$h_{m,ray} = \frac{\dot{q}''_{rad}}{C_p(T_g - T_s)} \tag{25}$$

where ρ is the density, α the thermal diffusivity, Nu the Nusselt number, l the local length scale above the condensed fuel surface and T_g gas temperature. Without combustion, the mass transfer number, B, is defined by the mass fraction of liquid equilibrium vapor, $Y_{F,s}$, which is obtained from the Clausius–Clapeyron equation [16].

$$B = \frac{Y_{F,\,\infty} - Y_{F,\,s}}{Y_{F,\,s} - 1} \tag{26}$$

where $Y_{F,\infty}$ is the fuel mass fraction in the free stream. Once ignition occurs due to the mixing between the fuel vapor and air, the mass transfer number, B, is defined by the heat of combustion [29].

$$B = \frac{H_c \nu_{F\,/\,O} Y_{O,\,\infty} + C_p(T_\infty - T_s)}{L_v + C_{pl}(T_s - T_0)} \tag{27}$$

where $\nu_{F/O}$ is the stoichiometric fuel/oxygen ratio, H_c the heat of combustion, C_{pl} the liquid specific heat and $Y_{O,\infty}$ and T_∞ are the oxygen mass fraction and temperature in free stream.

The pyrolysis model of the composite material needs effective material properties for properly estimating the thermal degradation of solid fuels in a fire situation. According to the experimental observation, a pyrolysis process of the composite material gives rise to a charred surface layer, and its thickness increases with time. The charred surface layer shields the heat flux and thereby limits the rate of fuel gas production. Advanced measurements on temperature-dependent, composite material property information on thermal conductivity, density, heat capacity, heat of pyrolysis and reactions Arrhenius parameters would require an extensive experimental effort. As a reference fuel material used in a cone calorimeter, only solid acrylic PMMA polymer has been widely used for assessing polymer flammability and characterizing the mass loss rate during combustion processes [30,31]. Furthermore, more comprehensive and complex models would be prohibitive in the framework of large CFD problems. In the current model, it is assumed that the virgin composite material decomposes to fuel gas through a single step solely over the surface of the composite material without considering the charred surface layer. This can be justified by the presence of a forced crossflow over the composite surface, which facilitates cracking of the charred layer and, as a consequence, results in a high pyrolysis rate by reducing the heat barrier layer [32]. The pyrolysis gas is in thermal equilibrium as in Equation (12), and the B-number approach as Equation (23) is taken here, expressly to test the robustness and efficiency of

such a type of model. Even with these simplifications, the number of properties needed is staggering, and we lack the ability to accurately quantify them here through bench-scale experiments. Table 1 presents the temperature-independent material property for the liquid fuel (kerosene) and the composite material used in fuselage.

Table 1. Material property for the liquid fuel (kerosene) and the composite material.

Property	Kerosene	Composite Material
Conductivity, k (W/m·K)	0.17	0.515
Density, ρ (kg/m^3)	750	1625
Heat capacity, C_p (kJ/kg·K)	2.45	2.015
Pyrolysis heat, L_v (kJ/kg)	256	9800
Combustion heat, H_c (kJ/kg)	44,000	21,000
Boiling temperature, T_B (°C)	216	–
Ignition temperature, T_{Ign} (°C)	–	390
Emissivity, ε	1	0.9

3. Results and Discussion

Large-scale (>10 m) liquid hydrocarbon pool fires are difficult to analyze experimentally because of the sheer scale of the fire. Several intermediate-scale pool-like fires [15,17,18] are taken here, expressly to test the robustness and efficiency of the model. Besides, it is a relatively easy task to obtain experimental data available for such fires for a detailed comparison between prediction and experiment. Simulations are performed on a multi-processor Linux cluster available at the Institut P' of Poitiers, using the parallel MPI [16].

3.1. Intermediate-Scale Fire

A free pool-like fire is stabilized on a horizontal rectangular porous burner [17] with a 0.25 m long (x) by 0.4 m wide (y) slot with a heat release rate of 36 kW. It is important to understand what characteristic length scale, which is related to the heat release rate (HRR), must be resolved. In general, the large-scale structure that is controlled by the inviscid terms can be completely described when the characteristic length is spanned by roughly ten computational cells [16]. For the fire plume considered here, the characteristic length is in an order of 0.25 m. This implies that adequate resolution of the fire plume at a large scale can be achieved with a spatial resolution of about 0.025 m in a 3D computational domain of 1.5(x) × 1(y) × 2(z) m^3. Based on this spatial reference value, the grid was locally refined in the fire region where a strongly stratified layer is developed. In the first case, the calculations were performed using a computational mesh with 62 cells in the direction x, 50 cells across (y) and 82 cells in the vertical direction (z). Along the axis x, start at 0.01 m in the combustion zone, and stretch to about 0.05 m at the free boundary. In the vertical direction, z, cell sizes are about 0.008 m around the burning zone and stretch to about 0.06 m at the free boundary. A uniform grid is used with a cell size of about 0.008 m in the y direction. Grid refinement studies were performed for checking the influence of the number of grid cells on the predicted results. In the second case, the number of grids with 82(x) × 60(y) × 102(z) was used (about 1.5-times as fine) with the extra grid points being added in regions of high velocity or temperature gradients. A further reduction in the grid size results in a large

computational overhead due to a significant reduction in the time step ($\Delta t < 0.001$ s), so that it satisfies the CFL [16] stability condition. The output from LES simulations had flow oscillations. The results from the computations were the time-averaged values over the range of the computational time (20 s). In the experiment [17], temperatures were obtained by means of fine wire thermocouples, and velocity and its fluctuation were determined using a two-component laser Doppler velocimetry (LDV) system. Profiles of the root-mean-square (RMS) value of the longitudinal velocity fluctuation, $w'w'$, and the transverse one, $u'u'$, obtained from the two grid systems at $z = 0.035$ m and 0.46 m, are compared with the experimental data in Figures 1 and 2. The calculated transverse velocity fluctuation, $u'u'$, is about 25% too low in the plume region ($z = 0.46$ m). Nevertheless, both the prediction and experiment suggest that the reacting flow field is displaced in a stronger flapping manner. Globally, the numerical model is capable of reproducing the mechanism generating the buoyant instability present in the early development of the flame ($z = 0.035$ m) and the transition to turbulence in the plume region ($z = 0.46$ m). Figures 3–5 show that the general shape of the experimentally-determined temperature and velocity profiles is correct. The computations over-predict the transverse velocity, u, at the fire base ($z = 0.015$ m) and underpredict the velocity and the temperature in the plume region ($z = 0.23$ m). These LES computations are practically grid independent. It can be concluded that the grid system determined from the fire characteristic length offers the best tradeoff between accuracy and cost for the present purpose.

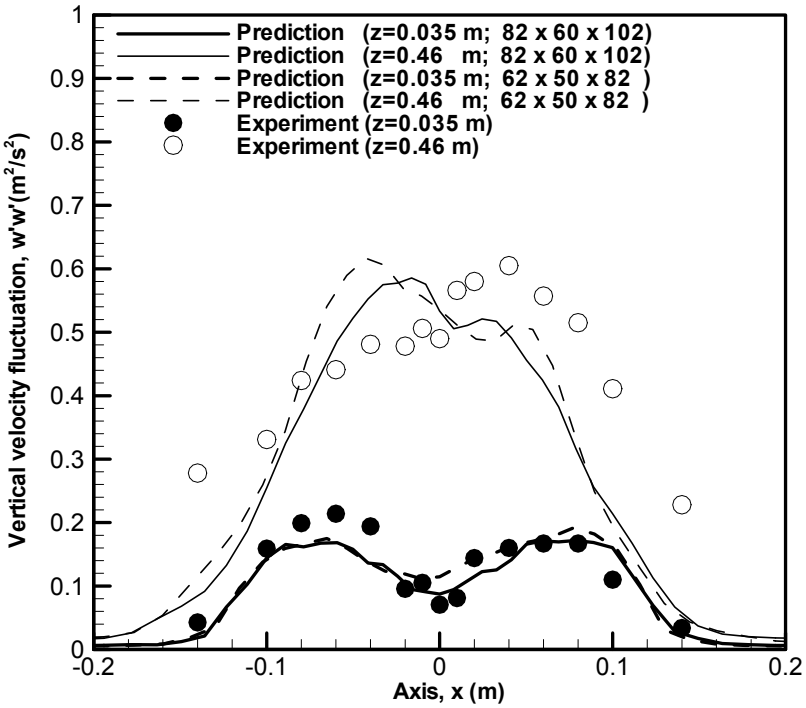

Figure 1. Profiles of the measured and predicted longitudinal velocity fluctuation, $w'w'$, at $z = 0.035$ and 0.46 m.

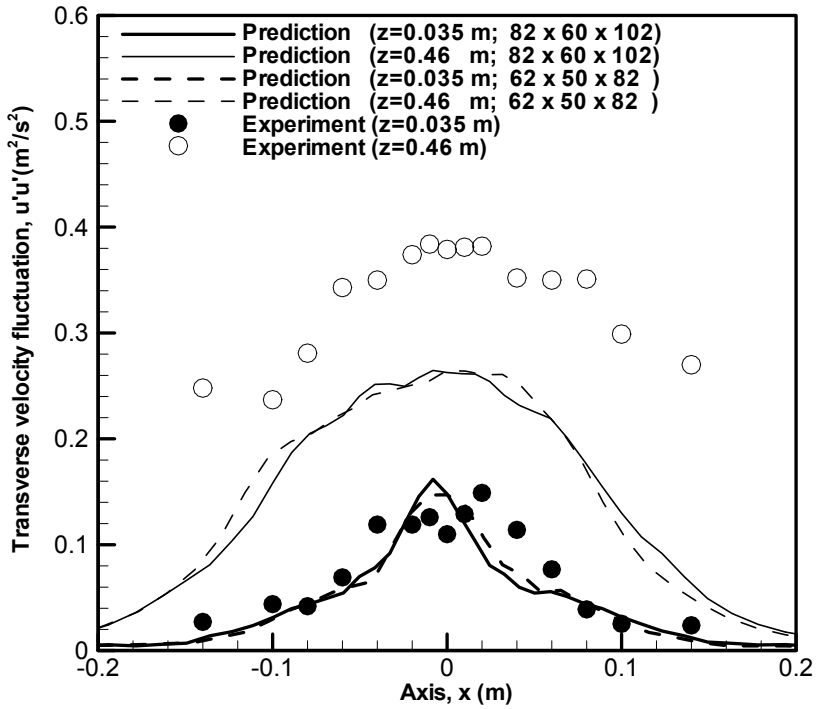

Figure 2. Profiles of the measured and predicted transverse velocity fluctuation, $u'u'$, at z = 0.035 and 0.46 m

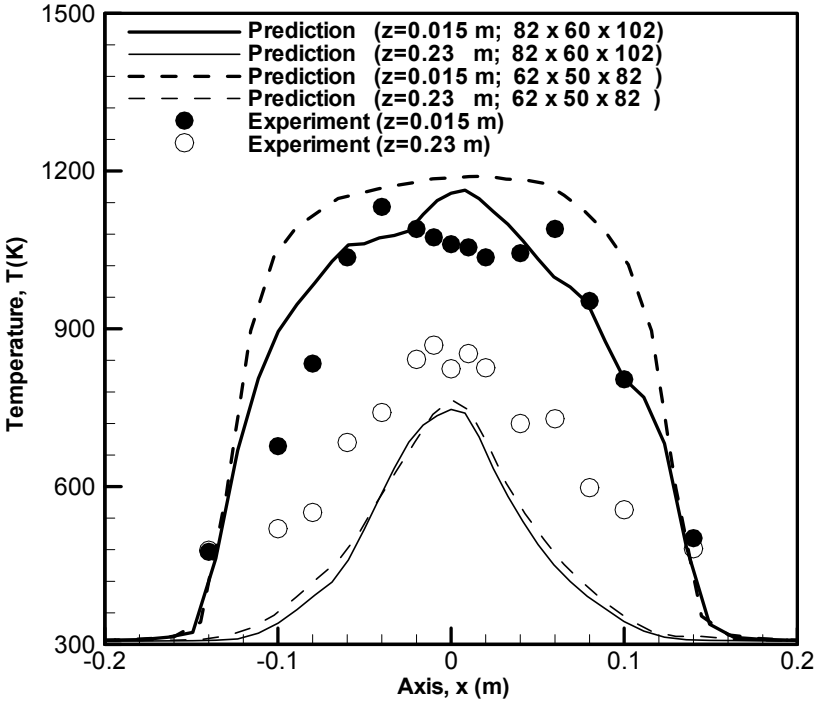

Figure 3. Profiles of the measured and predicted temperature at z = 0.015 and 0.23 m.

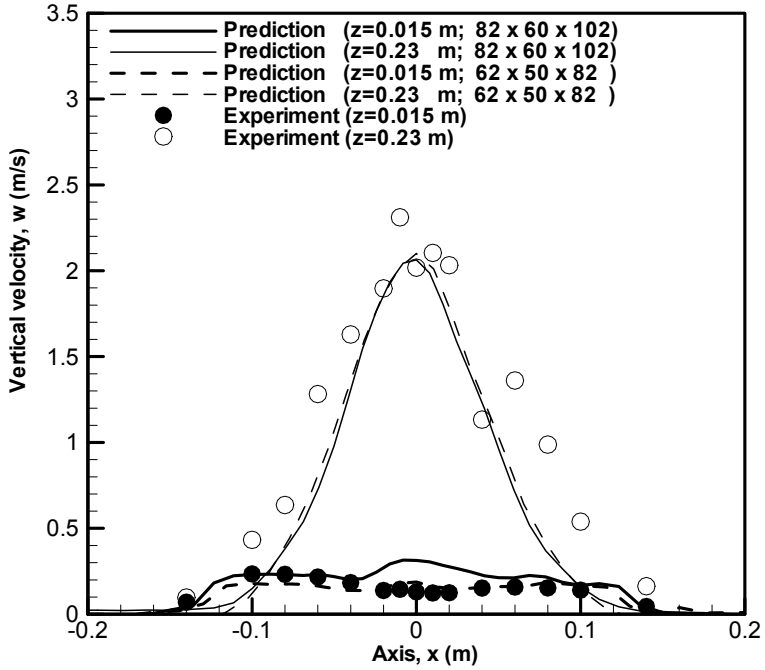

Figure 4. Profiles of the measured and predicted longitudinal velocity at z = 0.015 and 0.23 m.

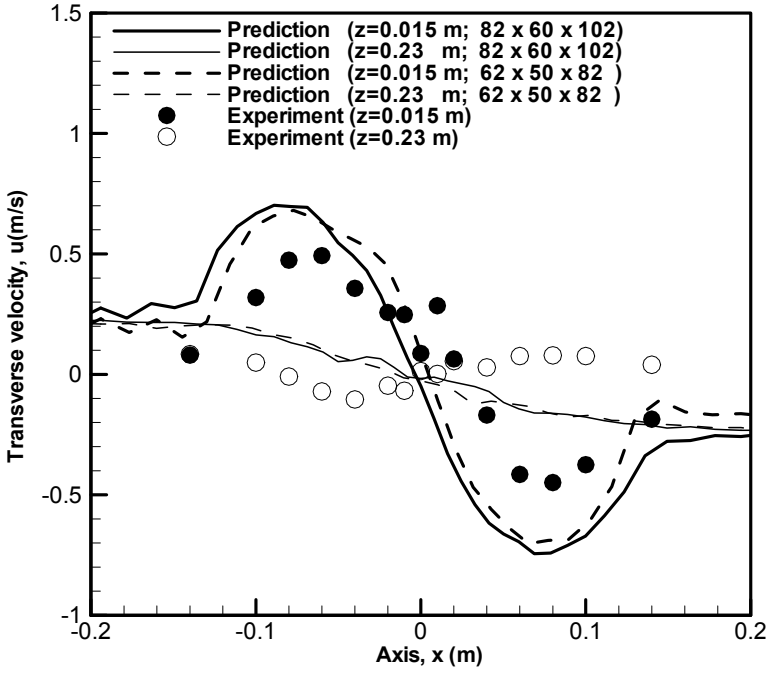

Figure 5. Profiles of the measured and predicted transverse velocity at z = 0.015 and 0.23 m.

Orloff [15] performed detailed measurement for the chemical species, such as CO and soot, from a low Froude number propane and propylene-free pool fire of 178 kW by using a porous burner of 0.75 m in diameter. Based on the fire characteristic length, a grid system containing 70(x) × 70(y) × 100(z) with uniform cell sizes of 2 cm is chosen. The predicted CO molar fraction in a traverse *versus* radial position at H = 5.2 cm and along the centerline against the average mixture fraction, Z, is plotted in Figure 6. The magnitude of CO is well predicted, and the computed profiles exhibit the same similarity that is observed experimentally. The peak in the carbon monoxide is predicted just inside the flame, and CO

declines significantly far away from the fire region. Turbulent mixing and fluctuations reduce the peak of CO concentrations as compared to that in laminar diffusion flames [15]. Both the experiment and prediction show that the local concentration of CO in the fire is correlated solely as a function of mixture fraction because buoyant turbulent diffusion flames at the intermediate scale generally have modest stretch rates. This implies that the CO generation depends essentially on the fuel type and is relatively independent of position in the over-fire region, of pool diameter and of heat release rate. The soot volume fraction *versus* radial position in a traverse position at $H = 0.12$ m above the propylene pool fire is shown in Figure 7. The predicted and measured profiles of soot show a high degree of similarity in the flame close to the fuel-rich condition ($Z > 0.1$). This implies that soot formation is likely subject to precursors, consistent with the hypothesis that the smoke point is the controlling parameter for soot formation. Past the flame tip, a significant amount of soot in the experimental flame [15] is not computed, particularly under the fuel-lean condition ($Z < 0.1$). That means that the transition from soot formation to oxidation occurs more quickly in the simulation than in the experiment, indicating that the model for the spatially-varying soot oxidation process needs adjustment. Besides, past the flame tip, soot surface growth may continue after its oxidation has ceased, causing a significant amount of soot to be sustained there. The influence of turbulent fluctuations, strong temperature and fuel-dependent effects on soot surface growth cannot be captured by the smoke-point concept in its present form. This helps explain the limited success of smoke-point attempts to predict soot emissions in fuel-lean conditions. The developed framework considers only the phenomena essential for obtaining sufficiently accurate predictions of chemical species and soot production in non-premixed turbulent flames of several engineering calculations. The Smagorinsky sub-grid model is known to be too dissipative, particularly for an insufficient grid refinement. An extremely small grid size (mm) is required to fully resolve the complex flow instabilities from a turbulent buoyant flame, making practical fire simulations difficult. Such a pulsing behavior also makes accurate measurements difficult. It seems most likely that the discrepancies are due to a combination of the experimental uncertainties and the possible error in the numerical simulation.

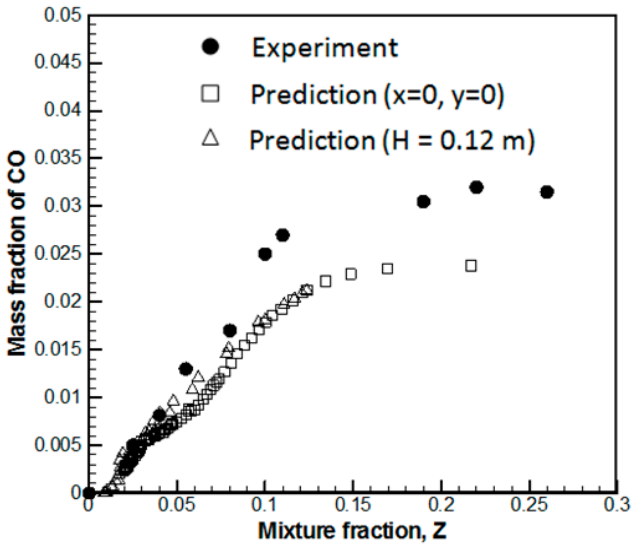

Figure 6. Comparison between the measured and predicted CO mass fraction as a function of the average mixture fraction

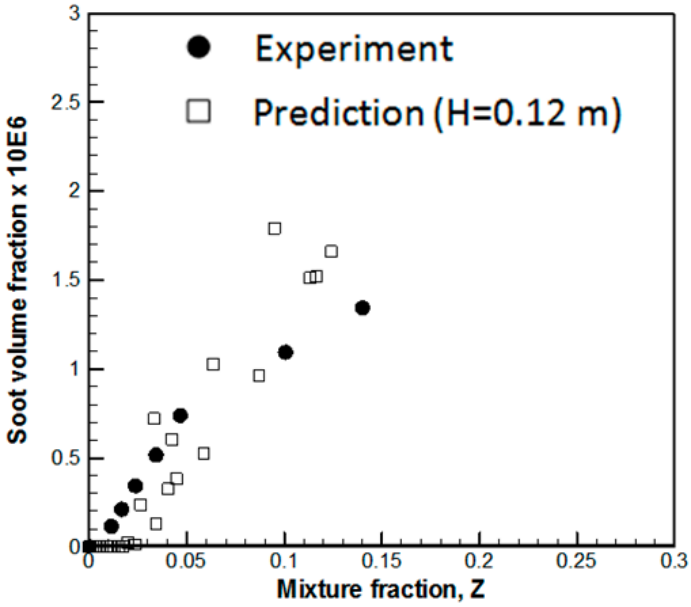

Figure 7. Comparison between the measured and predicted soot volume fraction as a function of the average mixture fraction at a height of 12 cm.

Kolb [18] performed measurements of the flame shape and heat flux on the median plane from a pool fire in crossflow with a velocity varying from 0.7 to 2 m/s, as shown in Figure 8. This fire with a heat release rate of 45 kW is supplied by using a propane burner with a length, x_b, of 0.25 m and a width of 0.4 m. Turbulent flames exhibit a pulsing behavior, and a mapping flame luminosity technique [18] using a CCD camera was developed to measure the visible flame shape through image processing using a selected luminosity threshold. This technique is based on the flame presence probability, and the mean flame length/height (X_f/H_f) are derived from the maximum flame ones (X_m/H_m) corresponding to the presence probability of 0.05 and the continuous ones (X_c/H_c) corresponding to the presence probability of 0.95. It was checked that the so-determined persistent flame shape can be defined as $X_f = 0.5(X_m + X_c)$ and $H_f = 0.5(H_m + H_c)$, corresponding to a gas temperature of about 450–500 °C. According to the experiment, for a heavily sooting flame, the visible flame shape corresponds to the zone where the gas temperature is higher than 500 °C. Determination of the visible flame extent with such a criterion (500 °C) is of particular concern in considering the ignition of adjacent objects by radiation and, as a consequence, the flame propagation. By using this criterion for determining the flame shape, the predicted flame height (H_f) and length from the leading edge ($L_f = X_f + 0.5x_c$) are compared with the experimentally-determined ones in Figure 9 as a function of crossflow velocity. Both the experiment and prediction show that the extent of the visible flame, L_f, progressively increases; however, the flame height decreases with an increase of the wind velocity. As compared to the experimentally-determined flame length, an overprediction of 10% for $U_0 = 0.5$ m/s and an underprediction of 20% for $U_0 = 1.5$ m/s are found. The flame at low wind velocity is roughly six-times thicker than that at high wind velocity, mainly due to buoyancy and air entrainment. If the stoichiometric coefficient (continuous zone) is used for determining the predicted flame shape, a big difference between the predicted flame shape and existing experimental data will be derived due to the different criteria. During experiment, the heat feedback to the wall was measured by mounting the radiometer aperture of a 150° view angle. The predicted and measured mean flame-surface heat flux downstream behind the burner ($x - x_b > 0$), along the burning

wall centerline (y = 0.2 m), is presented in Figure 10a,b. In spite of the discrepancy, the magnitude and distribution of the heat flux closely follow the general behavior of the experimental data in a range of wind velocity from 0.7 to 2.5 m/s. Just downstream behind the burner ($x - x_b < 0.25$ m), the total heat flux is found to decrease with an increase of the wind velocity due to a reduction in the flame thickness. Far away from the burner ($x - x_b > 0.5$ m), the total heat flux, as a whole, is proportional to the wind velocity mainly due to an increase of the flame extent. Rigorous comparison between prediction and measurement is again difficult for the buoyantly-controlled flame, which produces oscillatory behavior in the flame structure in a cyclic fashion, yielding the measurement error with an uncertainty of 10%–15%.

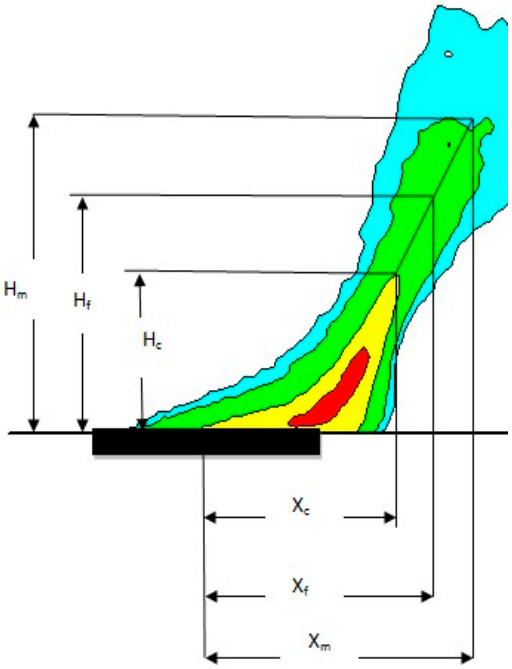

Figure 8. Pool fire in the crossflow and definition of the visible flame shape on the median plane.

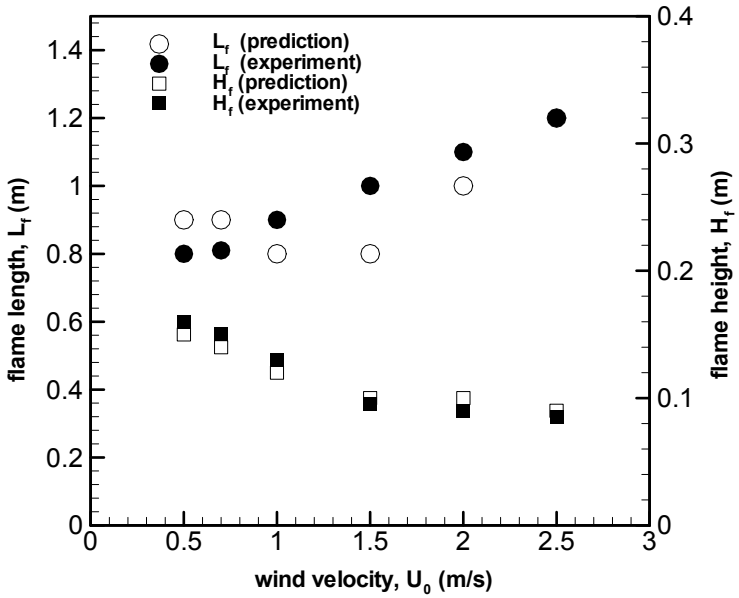

Figure 9. Comparison between the predicted and measured flame height/length as a function of the wind velocity.

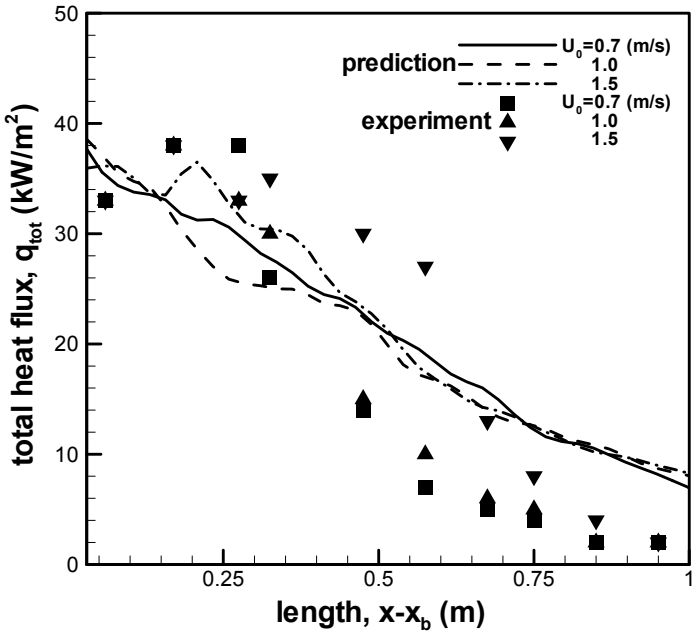

Figure 10. Comparison between predicted and measured total heat flux from the flame to the wall surface downstream behind the burner. (**a**) Heat flux for U_0 = 0.7, 1 and 1.5 m/s; (**b**) heat flux for U_0 = 2 and 2.5 m/s.

3.2. Large-Scale Fire

A schematic diagram of a post-crash pool fire (D = 20 m) engulfing a composite-type aircraft (for example, A350) and the coordinate system in the numerical simulation are shown in Figure 11. The calculations were performed using a computational mesh, which was made up of 200 × 200 × 250 cells with an overall dimension of 90 m in length (x), 90 m in width (y) and 100 m in height (z). The grid is locally refined, with extra grid points being added in strong shear stress zones, such as near the pool fire

surface and in the wake region around the aircraft. Along the length, *x*, cell sizes start at 0.15 m around the pool fire and stretch to about 1 m at the free boundary. In the z direction, cell sizes are approximately 0.1 m in the vicinity of the burning zone and stretch to about 1.2 m near the free boundary. A uniform grid is used with a cell size of approximately 0.45 m in the transversal direction, y. In general, the fire dynamic behavior at a large scale is qualitatively correct when the aspect ratio of cells is below 5, as proposed by FDS [16]. Upon encountering the perturbation induced by an aircraft in the crosswind, the boundary layer probably changes rapidly from transition into a fully turbulent one. The viscous sublayer is critically dependent on the near-wall model due to important viscous effects. An extremely small grid size (mm) is required to fully resolve the turbulent boundary layer and the complex flow instabilities in the wake around the aircraft for the high Reynolds number flow, making practical fire simulations difficult. In the present work, the computational nodes immediately adjacent to a wall are located in the fully turbulent region, and this simplicity allows faster computations and, by this, a higher spatial discretization and an increase of the resolved part of the fire oscillation. Besides, predictions of the most dominant radiative heat transfer are generally less sensitive to the near-wall turbulence model. It was found that the mildly-stretched grid system with a moderate computational domain offered the best tradeoff between accuracy and cost. With the use of a highly-compressed grid system, the build-up of numerical error could produce spurious results over the course of an LES calculation due to commutation of the filtering operation. Up to now, investigations of a large-scale fire are limited to computations on relatively coarse meshes everywhere [4,14].

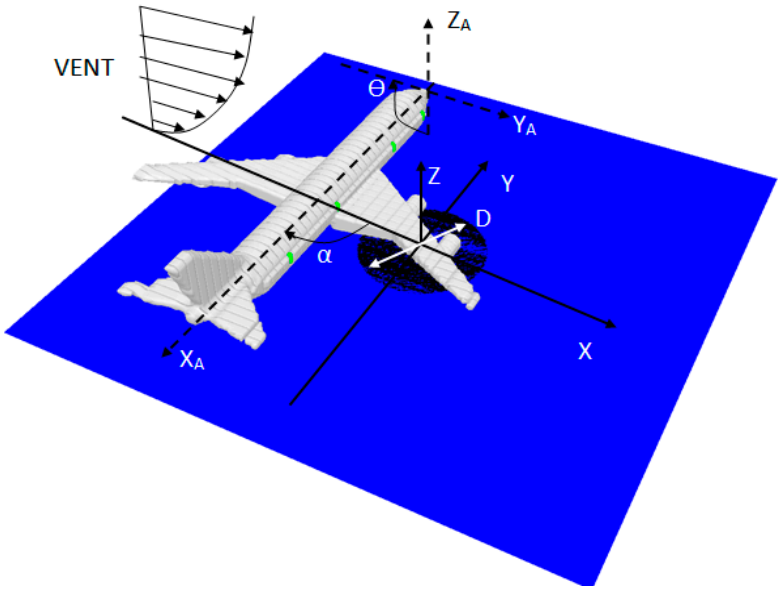

Figure 11. Schematic diagram of the occurrence of large fires engulfing an aircraft and the coordinate system in the numerical simulation.

The atmospheric condition, characterized by fluctuations in wind speed and direction, cannot be taken into account in the current simulation. The composite-type aircraft orientation relative to the external post-crash fire in the crosswind, the area of spill and the volume of fuel are the important parameters. Therefore, the scenarios of an aircraft post-crash fire are highly variable, because of the extremely varied nature of wind conditions. Therefore, the influence of deviation in the wind speed on the behavior of the fire is studied by taking into account a speed range of 0–10 m/s. The effects of aircraft orientation relative

to the wind direction, characterized by an angle α that varies from 0° to 360° (*cf.* Figure 11), on the major changes in the overall flame structure and, consequently, the heat flux on the fuselage skin, are also taken into account.

3.2.1. Instantaneous View of the Thermal Plume

The instantaneous shape of the flame where the gas temperature is higher than 500 °C, from the liquid fuel in the plane perpendicular to the fuselage for two wind speeds (U_0 = 2 and 10 m/s), is illustrated in Figure 12a,b. Surrounding the cone of fuel vapor is a zone of luminous persistent flame. Above this zone is a further combustion region, but here, there is intermittency and obvious turbulence in the flaming. Finally, there is the non-reacting buoyant plume, which is generally turbulent in nature and characterized by decreasing velocity and temperature with height. Wake regions are formed around aircraft, and at times, spiraling vortex flows are seen in the plume. For a low Froude (ratio between buoyant and inertia forces) number flame (U_0 = 2 m/s, Figure 12a), shear-stresses between hot combustion products and fresh air make the flow unstable and amplify oscillations near the fire base due to air entrainment variation and flame flicker, inducing large eddy structures corresponding to hot gas puff burning. Fresh air entrained by these vortexes feeds the flame with oxygen and cools the smoke, influencing natural convection and then air entrainment. In the natural convection limit, as the Froude number increases (U_0 = 10 m/s, Figure 12b), coherent structures appear also surrounding the cone of fuel vapor, the flame presenting a pronounced instability due to crossflow. The wind effect is the tilting of the plume, such that there are times when the aircraft is not fully engulfed by the flame. There are other complications deriving from the intermittency of the behaviors, with luminous regions of efficient combustion appearing randomly on the outer surface of the fire according to the turbulent fluctuations in the fire plume.

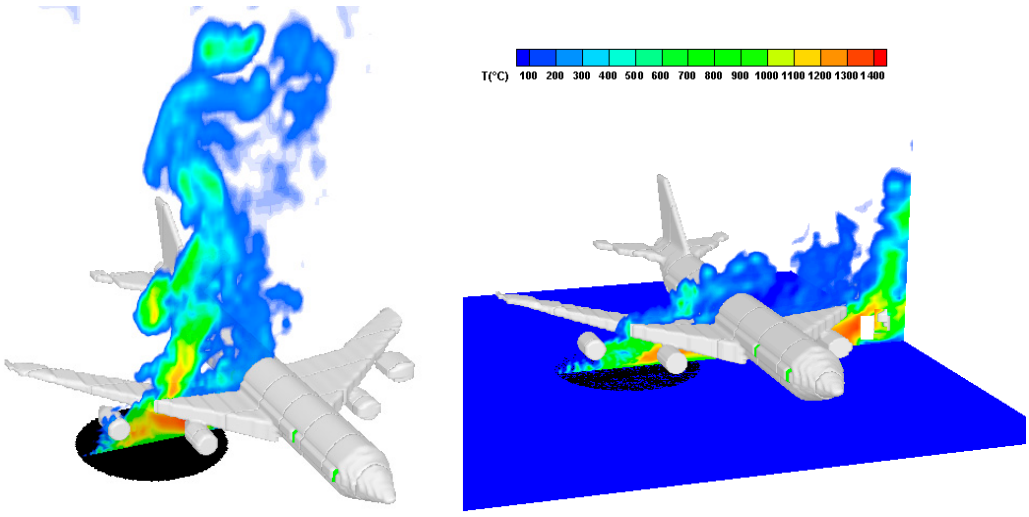

(**a**) (**b**)

Figure 12. Instantaneous view of the predicted thermal plume. (**a**) Low wind speed of 2 m/s; (**b**) high wind speed of 10 m/s.

3.2.2. Time Averaged Thermal Plume

The time-averaged temperature, CO molar fraction and soot mass fraction on a wind-assisted liquid fire engulfing an aircraft are presented in Figures 13–15. The time period over which the computation outputs were averaged from the last 60 s is considered as a quasi-steady period. It should be noted that for such a large-scale kerosene pool fire in crossflow, there is no link between the carbon monoxide concentration and the mixture fraction. The prediction suggests three main behaviors under a variety of wind conditions.

1) Under a quiescent condition, the main part of the flame, *i.e.*, the primary flame zone, is essentially vertical, as shown in Figure 13a. The quiescent fire consists of a buoyancy-dominated flame zone with a peak temperature of 1400 °C. The pool fire is located near the fuel source and far away from the aircraft. There is an excess of fuel due to the degradation of the composite material over the wing skin. This situation induces an increase in the thermal plume volume with time during the fire growth stage, containing large CO (*cf.* Figure 14a) and soot (*cf.* Figure 15a) with a peak value of 10% in the mass fraction.
2) With the presence of a low wind speed (*cf.* Figures 13b, 14b and 15b at $U_0 = 2$ m/s), the crossflow is significantly deflected near the fire source as a result of an enhanced thermal blockage by the buoyancy forces. Air entrainment and wind velocities can be of the same order of magnitude. The wind restricts the flow of entrained air and produces highly-mixed and, therefore, highly-combusting regions below the wing adjacent to the pool of the liquid fuel. However, the magnitude of the wind speed is insufficient to direct the flame towards the fuselage, and to reduce the CO and soot levels in the plume region.
3) For the medium wind speed (*cf.* Figures 13c, 14c and 15c at $U_0 = 5$ m/s), the flame is elongated in the downstream direction, and the region directly surrounding just in front of the aircraft is immersed in the highly-combusting zone with a peak temperature of 1300 °C due to complex wind/vorticity interactions. Flow is moving over the top of the aircraft, creating streamwise vortices, while fuel-rich air is forced below the fuselage. This situation induces an increase of the flame cover with a temperature level of about 700 °C, accompanied by the presence of CO and soot on the upper leeward side of the aircraft. It is found that the presence of a composite-type aircraft instead of an aluminum type one results in a significant increase of approximately one time in the temperature level over the top of the aircraft. Besides, on the leeward side of the aircraft, the enhanced convective transport, as a whole, leads to a significant amplitude of temperature (1300 °C), of the CO molar fraction (5%) and of soot mass fraction (7%).
4) The high wind speed ($U_0 = 10.2$ m/s) enhances the interaction between the crossflow and aircraft and, consequently, facilitates the global flame shape alterations (*cf.* Figure 13d), which are combined with global enhancements in turbulent mixing. The windward flow is strongly accelerated over the top of the aircraft, allowing the suppression of the flame cover ($T < 300$ °C), CO and soot due to increased convective transport. Besides, the fuel-rich flow is ejected from underneath the aircraft, and this creates a second high temperature zone (1400 °C) accompanied by large CO (*cf.* Figure 14d) and soot (*cf.* Figure 15d) productions (10% in mass fraction) on the leeward side of the aircraft due to enhanced mixing by the presence of the vortices in the wake

behind the aircraft. The magnitude of the wind speed is sufficient to direct the flame to the bottom surface of the fuselage, causing an excess of the fuel gas due to the pyrolysis of the composite material over the fuselage skin. The oxygen within the gap is insufficient to consume the fuel accumulated inside the gap, and the combustion within a vitiated gap is probably close to the rich limit of flammability with a flame temperature of about 1200 °C.

Overall, the predicted trend is consistent with the experimental findings of Suo–Anttila [5,6] from a large fire engulfing a cylindrical objet in the crosswind. The length of flame base drag (T > 1200 °C) is approximately one-time the pool size for the medium wind speed (U_0 = 5 m/s) and up to 1.5-times the pool size for the highly ventilated (U_0 = 10 m/s) fire. In a given deployed position of aircraft related to the direction of incident wind, the most straightforward changes in the flame geometry as a function of the magnitude of the wind speed are numerically reproduced.

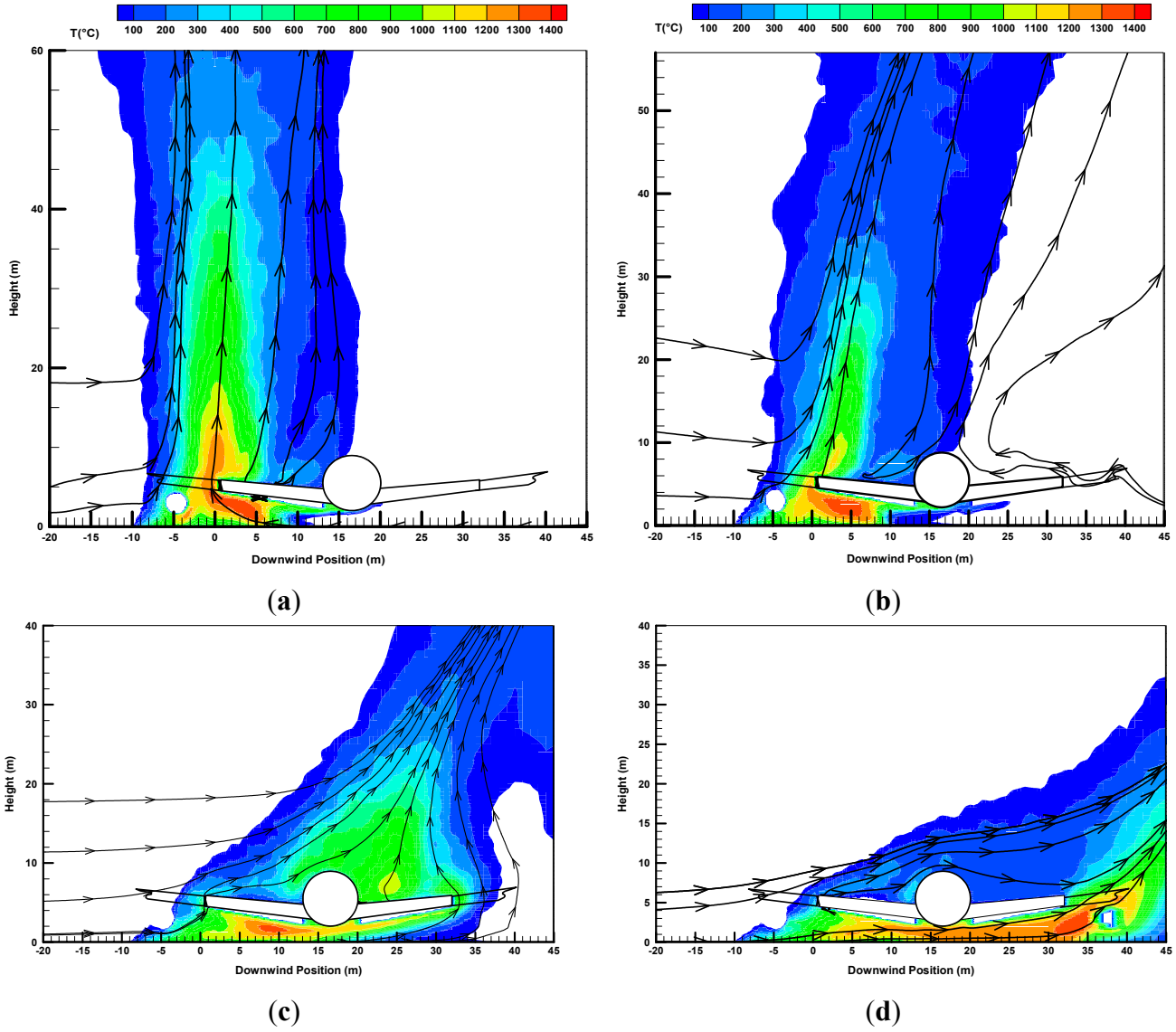

Figure 13. Contours of the time-averaged temperature for fires containing an aircraft of the composite type. (**a**) Quiescent condition; (**b**) low wind speed of 2 m/s; (**c**) medium wind speed of 5 m/s; (**d**) high wind speed of 10 m/s.

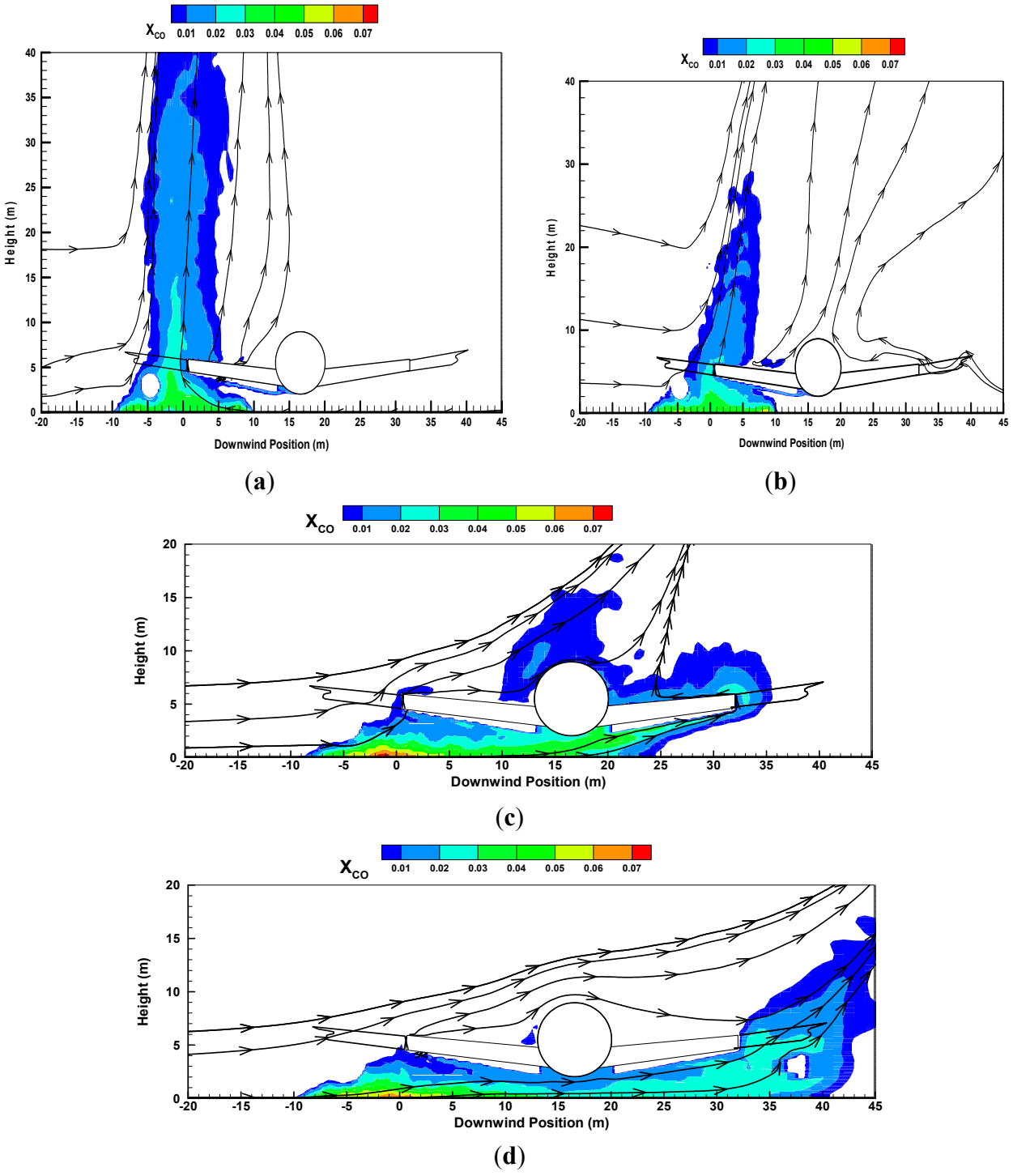

Figure 14. Contours of the time-averaged CO molar fraction for fires containing an aircraft of the composite type. (**a**) Quiescent condition; (**b**) low wind speed of 2 m/s; (**c**) medium wind speed of 5 m/s; (**d**) high wind speed of 10 m/s.

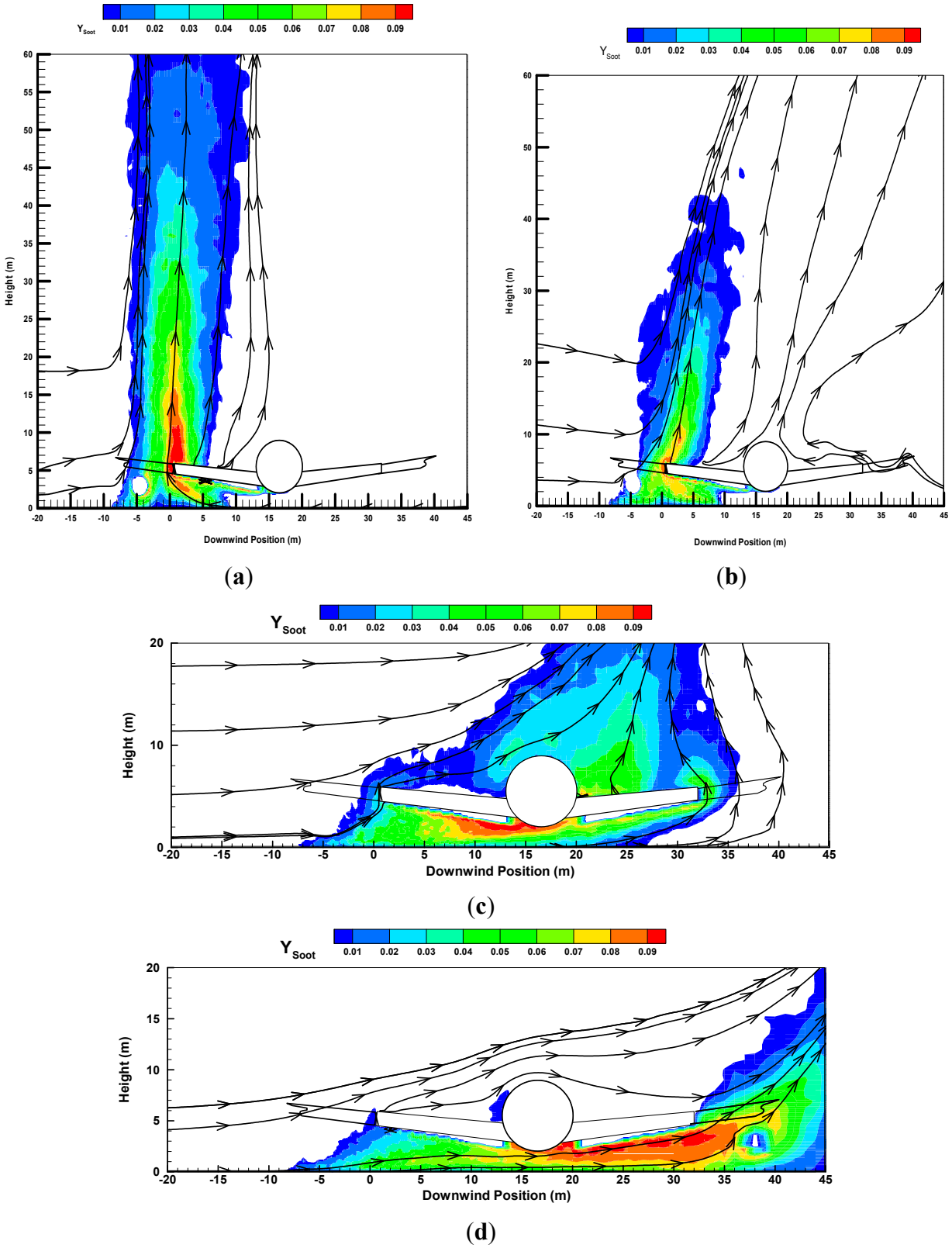

Figure 15. Contours of the time-averaged soot mass fraction for fires containing an aircraft of the composite type. (**a**) Quiescent condition; (**b**) low wind speed of 2 m/s; (**c**) medium wind speed of 5 m/s; (**d**) high wind speed of 10 m/s.

3.2.3. Heat Flux Distribution on the Fuselage Skin

For a large-scale fire, radiation flux seems the central and dominant mode of heat transfer, convection flux playing a secondary role [24]. The wind direction directly affects the view factor from the flame to the fuselage skin and, consequently, the maximum heat flux. The peak in heat flux is the highest when the aircraft moving direction is perpendicular to the crosswind ($\alpha = 270°$). The radiation heat flux to the surrounding fuselage skin depends mainly on three factors: (1) the flame volume and its temperature level; (2) the concentrations of gaseous and particulate soot emitting species; (3) the view factor from flame to the exposed fuselage skin.

Turbulent flames exhibit a pulsing behavior, and the oscillatory nature of the incident heat flux on the surface of the fuselage within the flame volume is always visibly apparent. The fluctuations demonstrate the effects of the characteristic large-scale turbulence of a free pool fire and wind. The fluctuations in heat flux for the medium wind speed are generally smaller than those for the low one. This phenomenon is believed to be due to the fact that the medium wind damps out the buoyancy forces in the flame. The time-averaged heat flux distribution over the fuselage skin in a quasi-steady period is the main parameters of interest, as illustrated in Figure 16a,b for medium (5 m/s) and high speeds (10 m/s). The heat flux on the fuselage skin is an increasing function of the intensification of the turbulent flame on the fuel-rich region. The heat flux on the fuselage skin is below 50 kW/m^2 for a wind speed below 2 m/s. This is due to the fact that the weak crossflow is deflected by the pool fire due to the buoyancy-induced air entrainment, and this prevents the flame from reaching the fuselage. In all of the cases, the flame height and its volume increase with the theoretical heat release rate, and the peak in heat flux on the fuselage skin becomes significant when the pool size exceeds 20 m.

For medium wind (*cf.* Figure 16a), the mean heat flux is considerably higher with a magnitude of 200 kW/m^2 on the windward side of the fuselage due to an impingement of the buoyant plume on the fuselage surface. The peak in heat flux is a factor of four increase relative to quiescent fires, and this trend is in agreement with the measured one for large fire [5,6,33]. The substantial thermal radiation develops also on the leeward side of the fuselage when it is immersed in a fire, resulting in a circumferential variation in the heat flux distribution. The heat flux increases to a maximum along the periphery to the underside of the fuselage. A dramatic horizontal variation in heat flux to the fuselage skin can be induced due to asymmetries in wind conditions, which cause the redirection of the flame zone by the wind component parallel to the axis of the fuselage.

The high wind speed of 10 m/s leads to a shallower smoke plume, and a region of increased heat flux to 200 kW/m^2 occurs only underneath the mock fuselage (*cf.* Figure 16b). A dramatic reduction in heat flux is brought about beyond that region due to the absence of the flame. The increase of the wind speed results in only an alteration of the distribution of the incident heat fluxes to the fuselage skin. It is found that the peaks in heat flux for the medium and high wind speeds are almost equal in magnitude. There are trends for the angular variation in heat fluxes: the bottom of the fuselage demonstrates the highest heat fluxes; the windward and leeward sides follow closely; and the upper part demonstrates the lowest heat fluxes. The minimum heat flux exists on the top of the fuselage, consistent with the thin flame cover there (*cf.* Figure 13d). As an illustration, the mean heat flux distribution over the wing skin is shown in Figure 17. The extent of the higher heat flux to the wing skin rises with an increase of the wind speed as a result of acceleration of the flow underneath the mock fuselage, creating a well-mixed region, which

can significantly strengthen the burning rate of the composite material. The fact that the heat flux values on the wing skin are higher indicates that an actively burning region over the wing surface is present. The magnitudes of the heat fluxes in excess of 240 kW/m^2 exist over the two wings' skin due to a large flame base drag (*cf.* Figure 6).

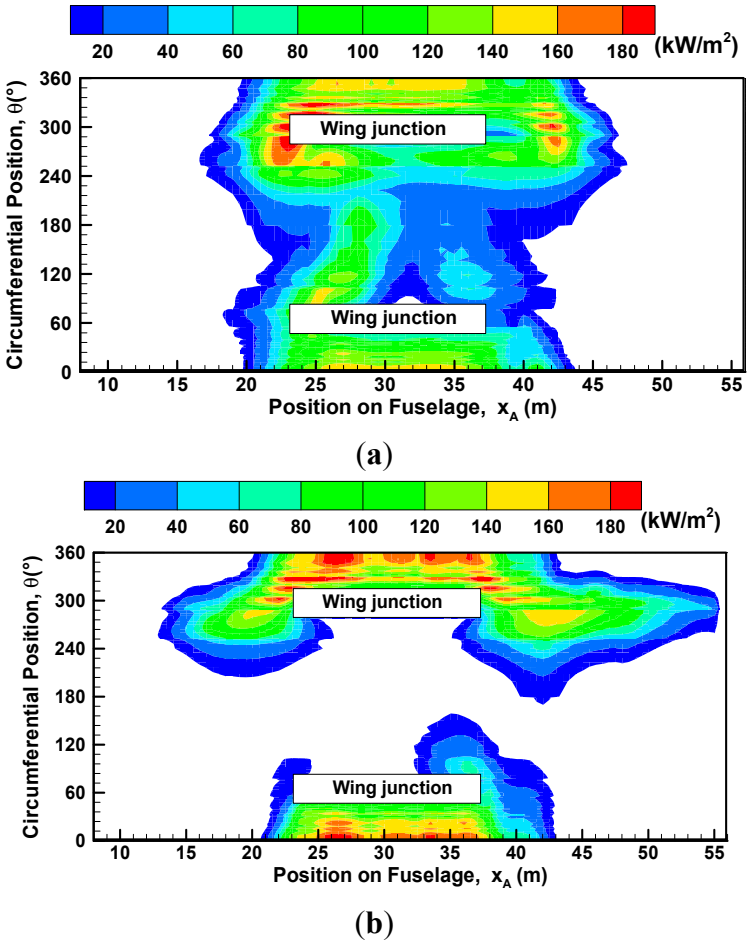

Figure 16. Iso-contour of the incident heat flux on the fuselage skin. (**a**) Wind speed of 5 m/s; (**b**) wind speed of 10 m/s.

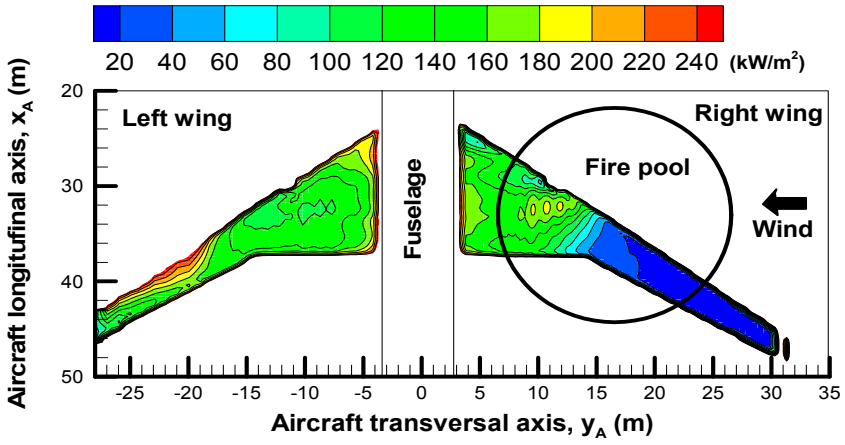

Figure 17. Iso-contour of the incident heat flux on the wings' skin.

3.2.4. Burning Rate over the Composite-Type Fuselage Skin

Changes in the maximum burning rate over the fuselage skin depend on the orientation of aircraft relative to the wind direction due to global flame zone redirection. The peak in the burning rate is the highest when the aircraft moving direction is perpendicular to the crosswind ($\alpha = 270°$). Iso-contours of the predicted burning rate on the fuselage skin in such a situation are illustrated in Figure 18a–d at various wind velocities. Over each side, the surface burning corresponds to a signal representing the presence of flames above the region. The circumferential variations in the surface burning are the result of fluctuating, not uniform temperature fields due to interaction between the buoyancy and inertia forces. A critical heat flux of 30 kW/m^2 is predicted, below which the pyrolysis enters the decay phase rapidly.

1) For the low wind speed ($U_0 < 2$ m/s, *cf.* Figure 18a,b), a burning rate higher than 15 g/m^2·s occurs only on the windward side as a result of the attachment of the actively-combusting region to the fuselage skin adjacent to the pool fire.
2) The resulting burning rate becomes tightly coupled to fire environment with the medium wind speed ($U_0 = 5$ m/s, *cf.* Figure 18c). The plume is displaced, which brings about a significant change to the radiation distribution and, hence, the vaporization rate of the composite material. This supports the postulation of an interaction between the aircraft and the fire that surrounds it. The burning rate with a magnitude of 12 g/m^2·s occurs on the windward side of the fuselage due to the impingement of the buoyant plume on the fuselage skin. The burning rate is the highest at the leeward side with a value of 16 g/m^2·s and decreases appreciably at the other sides. A substantial thermal radiation takes place on the leeward side of the fuselage when it is immersed in a fire, resulting in a moderate circumferential variation in the burning rate.
3) For the high wind speed (*cf.* Figure 18d), a magnitude of the burning rate in excess of 20 g/m^2·s exists on the leeward side of the fuselage due to a large flame base drag (*cf.* Figure 13d). The predicted fuel recession rate of composite material follows closely the one measured during the course of the experiment in a cone calorimeter. The minimum burning rate exists on the top of the fuselage, consistent with the thin flame cover there. The mass loss rate over the top surface of the fuselage suggests an inverse dependence with the wind velocity beyond 5 m/s.

The history of the global mass loss rate of the composite material averaged over the total pyrolysis surface is presented in Figure 19 at various wind speeds. It is seen that during the flame spread period, the mass loss rate increases quickly when an actively-burning region over the composite surface is present and is generally higher at strong wind velocity. For a wind speed below 2 m/s, the flame stands up into a plume in front of the aircraft under a buoyancy-controlled condition, and hence, about 80 s are required to start the degradation of such a composite material. The increase of the wind speed strengthens the degradation of the composite-type fuselage significantly due to the enhanced impact of the flame on the fuselage skin. When the ratio (Froude number) of the inertia force to the buoyancy one is great for a wind velocity beyond 5 m/s, only 10 s is sufficient for starting the degradation of the composite material. When the flame propagation is fully developed, the heat release rate reaches its maximum value. During the steady-state period, the burning rate per unit area of composite material increases with wind speed up to 2 m/s, beyond which limit it becomes largely independent of wind. This dependence is related to

the burning regime, which becomes increasingly dominated by radiation as soot levels rise up to a value where the fire is effectively optically thick and saturated.

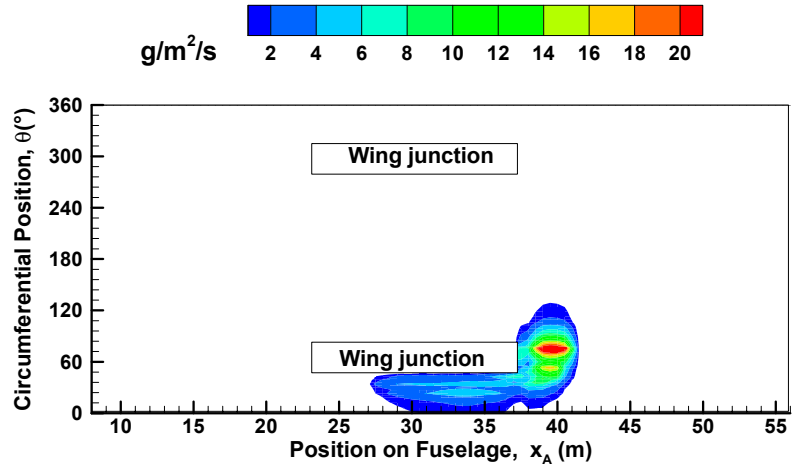

(**a**)

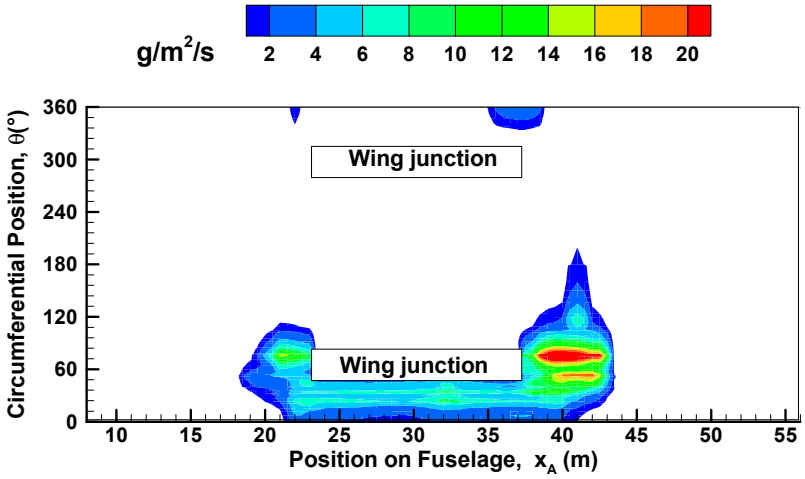

(**b**)

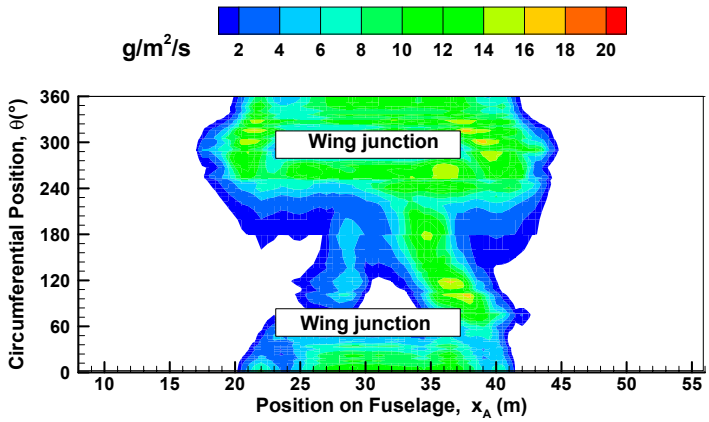

(**c**)

Figure 18. *Cont.*

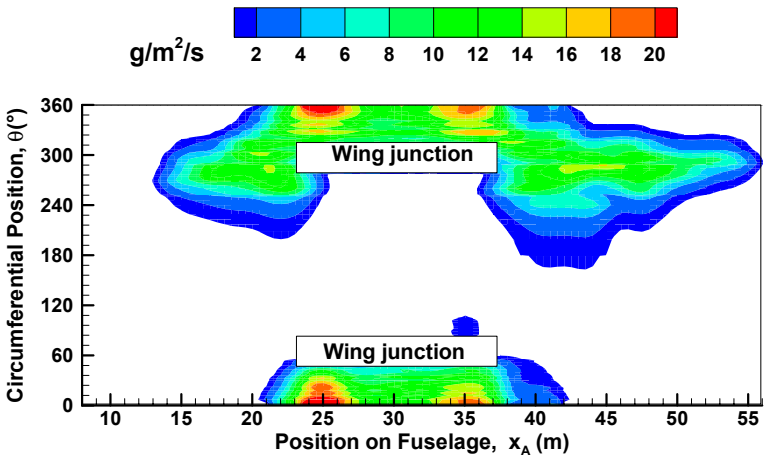

(**d**)

Figure 18. Iso-contours of the mass loss rate over the skin of the composite-type fuselage with a wind direction of 270°. (**a**) Quiescent fire condition; (**b**) low wind speed of 2 m/s; (**c**) Medium wind speed of 5 m/s; (**d**) high wind speed of 10 m/s.

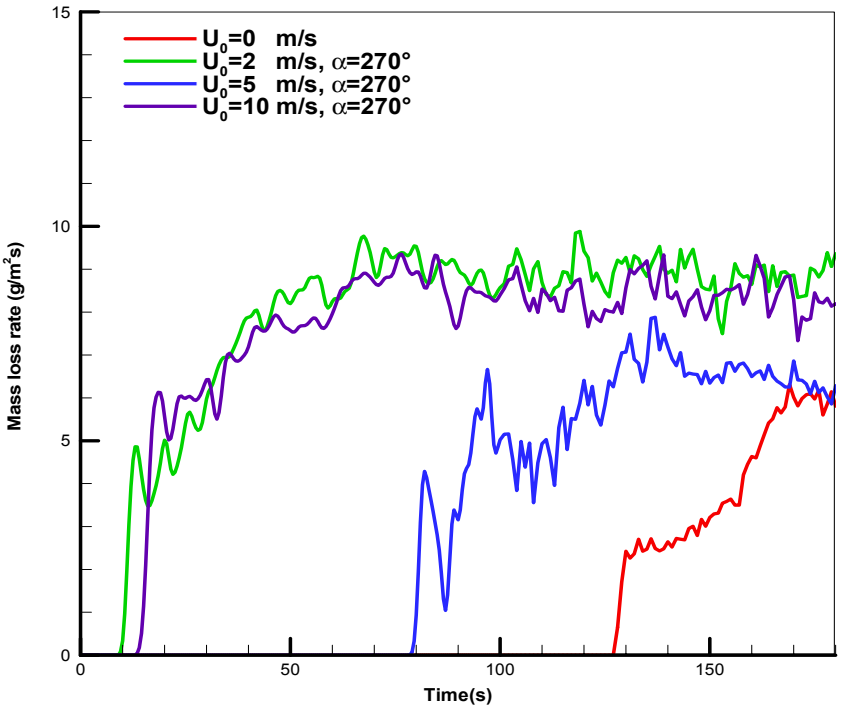

Figure 19. History of the mass loss rate of the composite material for the different wind speeds.

3.2.5. Burning Rate of the Liquid Fuel

These analyses consider a liquid pool fire burning at steady state after the initial stages of a fire. The heat feedback from the flame to the liquid pool surface directly affects the liquid heating rate to its boiling point of about 220 °C and, consequently, its vaporization rate. The history of the mass loss rate of liquid fuel for the different wind intensities is presented in Figure 20. The global regression rate is found to increase from 60 g/m^2·s to a value of approximately 70 g/ m^2·s with a rise of the wind velocity to 2 m/s. A further increase of the wind speed to 5 m/s strengths the mixing of the reactants and induces the most rapid regression of the liquid fuel as a result of the enhanced heat flux. Several studies show

significant increases in the burning rates of large open-air liquid pools with increased wind [34]. The high wind speed of 10 m/s greatly attenuates radiative feedback to the liquid fuel surface due to reduction in the flame cover, thereby depressing the mass burning rate. Besides, the oxygen below the fuselage is particularly low due to the accumulated fuel inside the gap, resulting in a decrease of the mass transfer number B and, consequently, of the regression rate (*cf.* Equation (23)). The mass loss rate of the liquid fuel is about 90 g/m^2·s for the wind speed of 5 m/s, which represents an increase of about 30% compared to that for a high speed of 10 m/s. The average fuel recession rate is about 6–7 mm/min as a function of the wind speed, which follows closely the fuel recession rate of 6.3 mm/min measured during the course of the experiment in a 9.1 m by 18.3 m pool [9].

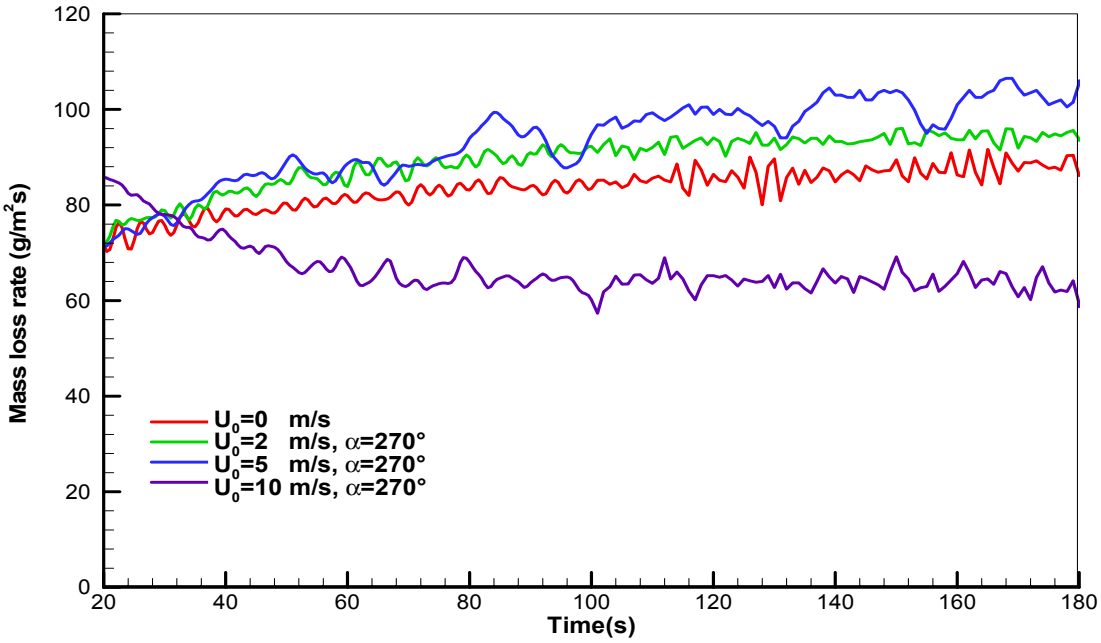

Figure 20. History of the mass loss rate of the liquid fuel during the fire propagation over the composite-type aircraft for the different wind speeds.

3.2.6. Heat Release Rate

The heat release rate for composite-type aircraft is the most intensive when the wind direction is perpendicular to the fuselage. The pyrolysis area of the composite-type aircraft increases with the wind speed during fire propagation. The ratio between the pyrolyzed area and the fuselage surface one is about 5% for the low wind speed (U_0 < 2 m/s) and reaches an asymptotic value of 30% for a wind velocity beyond 5 m/s. The turbulent nature of the flow brings fuel to the outside, where it can be combusted more efficiently, to release pluses of much more powerful energy from the flames. The history of the heat release rate (HRR) generated from the pool fire for different wind speeds is shown in Figure 21. Globally, the total supply of energy is elevated or depressed depending on the local air-to-fuel ratios and the efficiency of mixing, affected by the wind condition. For the wind speed below 5 m/s, the heat release rate is closely correlated to the trend of the regression rate of liquid fuel. For the quiescent pool fire, the buoyancy-induced air entrainment provides a mixing of fuel to air, and the contribution of the pyrolysis of the composite material to the total heat generation is practically negligible as compared to the liquid

fuel, exhibiting the lowest HRR of about 1000 MW. The high wind can alter the flame shape, as well as pyrolysis zone over the fuselage and wing skins and the entrainment phenomena. The high wind-assisted fire exhibits the highest HRR of about 1500 MW due to the large contribution of the pyrolysis of the composite material over the wing skin (*cf.* Figure 17).

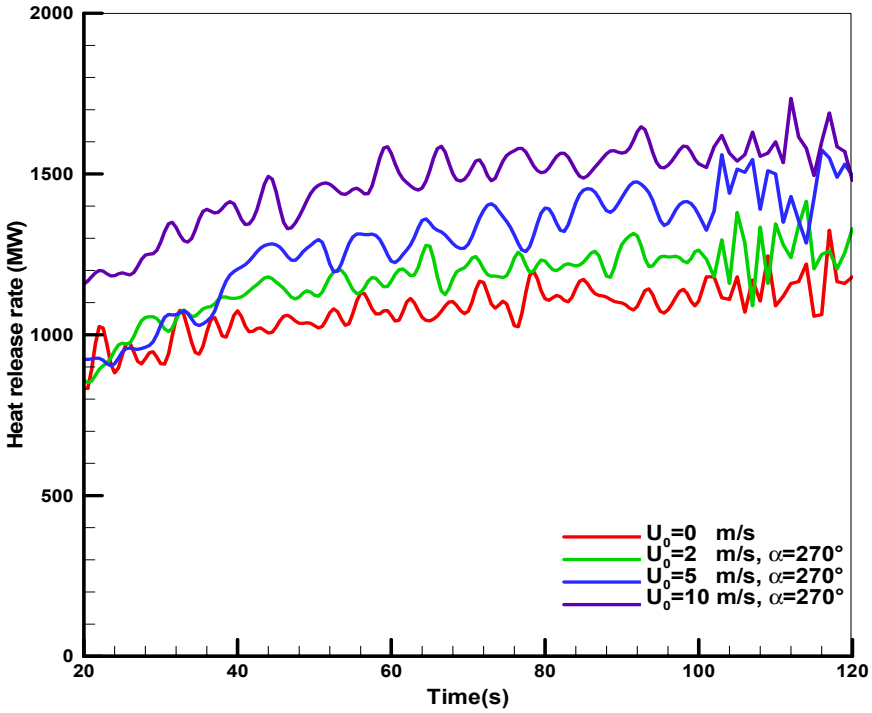

Figure 21. History of the heat release rate during the fire propagation over the composite-type aircraft for the different wind speeds.

3.2.7. Flame Spread Rate over the Fuselage Skin

During a fire, a thermal layer containing the hot gases and soot is transported by natural or forced convection. The composite-type fuselage is gradually heated up to its ignition temperature of 390 °C by applying a heat flux up to 240 kW/m^2 from the pool kerosene fire. The gaseous products from pyrolysis of the composite materials in contact with air ignite in the flammability limits. The flame spread occurs as a result of heating of the unignited part of the fuel surface to an ignition temperature at which the pyrolysis flux exceeds a certain threshold level, essentially dependent on air crossflow. An expression for the flame spread velocity, defined as the pyrolysis front advancement rate, is derived from the following expression, $V_f = dx_p/dt$. The time for the temperature at a given position over the composite material surface to reach the ignition temperature is selected for the pyrolysis front arrival time, dt, for calculating the pyrolysis spread rate. Temporal data, as plotted in Figure 22 for the different wind velocities, are important in the presentation of the flame spread information, because changes in the flame propagation can be correlated with events in the fire affected by the wind condition. The high wind speed brings about important mixing and more efficient combustion, which tends to increase the flame spread rate. The numerical results suggest that the flame propagation over the composite material surface occurs in two successive modes. In the first mode corresponding to the preheating processes of the composite material, the flame spreads slowly over the fuselage skin with a mean value of 8 cm/s.

The second mode is evident from a sharp rise of the flame spread rate up to 0.6 m/s in the slope of the curves due to the thermal exposure of the fuselage skin immersed in the fire environment and seen to occur at t = 15 s. Later, the flame spread rate V_f is essentially constant with a value of 5 cm/s when the fire propagation over the fuselage skin reaches a steady state.

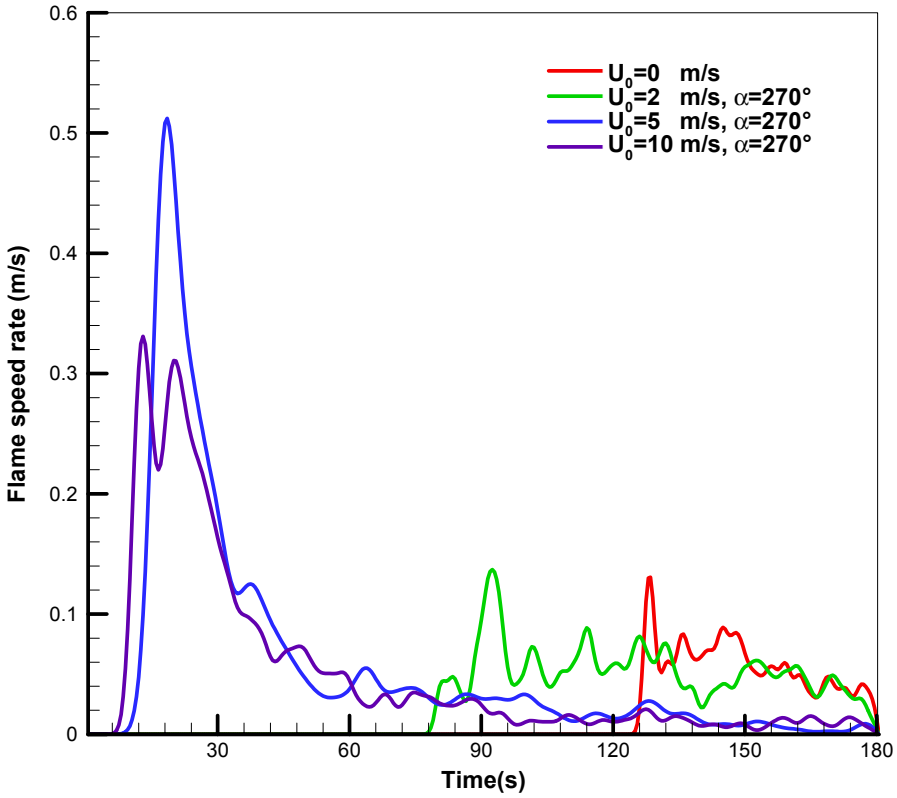

Figure 22. History of the flame spread rate over the skin of the composite-type fuselage for the different wind speeds.

4. Conclusions

A numerical study was conducted to supply information about the thermal exposure of a large object immersed in a fire environment. Heat flux and temperature fields have been studied in a variety of ways, and the strong influence of the wind has been noted. The largest factor affecting the reproducibility of the thermal environment in a large free pool fire is the wind conditions. The current model considers only the phenomena essential for obtaining sufficiently accurate predictions of heat flux and temperature field to make CFD calculations of large-scale fire feasible in an engineering context. The EDC-based combustion model and the common sub-grid scale turbulence model are satisfactory for the buoyancy-controlled fire in the crosswind. The CFD approach is much more realistic, when dealing with the characteristics of the wind-induced interaction of fires and large objects, than the simpler alternatives. The importance of considering the presence of an aircraft in fire is due to the coupling that occurs between the object size, shape, location, orientation and the fire environment.

The influence of the wind speed and the positioning of the aircraft in luminous flames on the heat flux to the fuselage skin is analyzed. The peak in heat flux to the composite fuselage skin ranges from 50 to 240 kW/m^2 as a function of the wind conditions, and the contribution of the radiation is higher than

95% of the total heat flux. The peak in heat flux to a medium or high wind is about a factor of four increase of that to a low wind speed. In the current work, activities have been confined also to calculation of the gas temperature and the toxic products. Increasing the wind leads to a shallower smoke plume, but does not help to suppress soot and CO around the engulfed aircraft.

It should be noted that the spread of fire assisted by a strong wind is the fastest mode of propagation and the most devastating in particular when the wind direction is perpendicular to the aircraft moving direction. Transition from the unsteady to the steady mode occurs earlier at high wind velocity ($U_0 > 5$ m/s) due to the flame impingement on the fuselage. However, at the steady mode, the flame spread rate is generally higher for the low wind velocity due to the flame radiation contribution from the buoyancy-controlled plume. These phenomena can be amplified by an increase in the pool fire size, and the deterioration of the pyrolysis zone is highly sensitive to the aircraft orientation relative to the wind direction. An increase of the pool size significantly enhances the pyrolysis zone over the fuselage skin, which, as a whole, is proportional to the wind speed.

Scenarios of a real large-scale fire are highly variable, because of the extremely varied nature of wind conditions, characterized by fluctuations in the wind speed and direction. The wind deviations in speed and direction are erratic in nature and contribute to the large spatial and temporal variations of the flame shape and heat flux distribution in a real large-scale fire situation. The negligence of the unavoidable deviations of wind speed/direction from their average values in the numerical simulation may induce large difference from the real fire situation for the mean flame shape and heat flux distribution. The predicted temperature and heat flux levels from a large-scale fire, although preliminary, are quantitatively correct only under a specific wind condition with a dominant speed and direction. Although the fire dynamic behavior at a large-scale is qualitatively correct, any attempt to draw a quantitative conclusion is discouraged due to the coupling of the extremely varied parameters, such as the atmospheric condition, aircraft orientation, area of spill and volume of fuel, *etc.* A more comprehensive pyrolysis model in addition to the wind effects on the vaporization rate of the composite material should be further investigated. Measurements of temperature, heat flux and toxic product from a real aircraft fire test would consolidate the insight provided by the CFD activity.

Acknowledgments

This study is sponsored by the European Project AirCraftFire under Contract Number FP7-2010-265612-CP.

Author Contributions

This work was performed by Guo Da Wang. Both the two authors analyzed the data and Hui Ying Wang wrote this paper.

Conflicts of Interest

The authors declare no conflict of interest.

References

1. Galea, E.R.; Markatos, N.C. A review of mathematical modelling of aircraft cabin fires. *Appl. Math. Model.* **1987**, *11*, 162–171.
2. Lavid, M.; Berlad, A.L. Gravitational effects on chemically reacting boundary layer flows over a horizontal flat plate. *Symp. Combust.* **1977**, *16*, 1557–1568.
3. Putnam, A.A. A model study of wind-blown free burning fires. *Symp. Combust*. **1965**, *10*, 1039–1046.
4. Sinai, Y.L.; Owens, M.P. Validation of CFD modelling of unconfined pool fires with cross-wind: Flame geometry. *Fire Saf. J.* **1995**, *24*, 1–34.
5. Suo-Anttila, J.M.; Gritzo, L. The effects of wind on fire environments containing large cylinders. *Combust. Sci. Technol.* **2011**, *181*, 68–77.
6. Suo-Anttila, J.M.; Gritzo, L. *Thermal Measurements from a Series of Tests with a Large Cylindrical Calorimeter on the Leeward Edge of a JP-8 Pool Fire in Cross-Flow*; SAND 2001-1986; Sandia National Laboratories: Albuquerque, NM, USA; Livermore, CA, USA, July 2001.
7. Lönnermark, A.; Ingason, H. Fire spread and flame length in large-scale tunnel fires. *Fire Technol*. **2006**, *42*, 283–302.
8. Russell, L.H.; Cannfield, J.A. Experimental measurement of heat transfer to a cylinder immersed in a large aviation-fuel fire. *J. Heat Transf.* **1973**, *95C*, 397–407.
9. Gregory, J.; Keltner, N.R.; Mata, R. Thermal measurements in large pool fires. *J. Heat Transf.* **1989**, *111*, 446–454.
10. Birk, A.M.; Oosthuizen, P.H. Model for the prediction of radiant heat transfer to a horizontal cylinder engulfed in flames. *Mech. Eng.* **1983**, *105*, 96.
11. Gritzo, L.A.; Nicolette, V.F. Coupling of large fire phenomenon with object geometry and object thermal response. *J. Fire Sci.* **1997**, *15*, 427–442.
12. Keltner, N.R.; Gill, W.; Kent, L.A. Simulating fuel spill fires under the wing of an aircraft. In Proceedings of the Fourth International Symposium on Fire Safety Science, Ottawa, ON, Canada, 13–17 June 1994; pp. 1017–1028.
13. Gottuk, D.T.; Rohy, R.J.; Beyler, C.I. Study of carbon monoxide and smoke yields from compartment fires with external burning. *Symp. Combust.* **1992**, *24*, 1729–1735.
14. Wang, H.Y. Prediction of soot and carbon monoxide production in a ventilated tunnel fire by using a computer simulation. *Fire Saf. J*. **2009**, *44*, 394–406.
15. Orloff, L.; de Ris, J.; Delichatsios, M.A. Chemical effects on molecular species concentrations in turbulent fires. *Combust. Flame* **1987**, *69*, 273–289.
16. McGrattan, K.; Hostikka, S.; Floyd, J.; Baum, H.; Rehm, R. *Fire Dynamics Simulator—Technical Reference Guide*; National Insitute of Standards and Technology: Washington, DC, USA, 2012; Number 1018.
17. Annarumma, M.O.; Most, J.M.; Joulain, P. On the numerical modeling of buoyancy-dominated turbulent vertical diffusion flames. *Combust. Flame* **1991**, *85*, 403–415.
18. Kolb, G.; Torero, J.L.; Most, J.M.; Joulain, P. Cross flow effects on the flame height of an intermediate scale diffusion flame. In Proceedings of the International Symposium on Fire Science and Technology, Seoul, Korea, 12–14 November 1997; pp. 169–177.

19. Baum, H.R.; McGrattan, K.B.; Rehm, R.G. Three dimensional simulation of fire plume dynamics. *J. Heat Transf. Soc. Jpn*. **1997**, *35*, 45–52.
20. Menon, S.; Yeung, P.K.; Kim, W.W. Effect of subgrid models on the computed interscale energy transfer in isotropic turbulence. *Comput. Fluids* **1996**, *25*, 165–180.
21. Chen, Z.B.; Wen, J.X.; Xu, B.P.; Dembele, S. The extension of eddy dissipation concept in the framework of Large Eddy Simulation and the subsequent modification. In Proceedings of the 23rd ICDERS, Irvine, CA, USA, 24–29 July 2011.
22. Dryer, F.L.; Glassman, I. High-temperature oxidation of CO and CH_4. *Symp. Combust*. **1973**, *14*, 987–1003.
23. Adiga, K.C.; Ramaker, D.E. Modeling pool-like gas flames of propane. *Fire Saf. J*. **1989**, *14*, 241–250.
24. Markstein, G.H. Radiative energy transfer from turbulent diffusion flames. *Combust. Flmae* **1976**, *27*, 51–63.
25. Beji, T.; Zhang, J.; Delichatsios, M.A. Determination of soot formation rate from laminar smoke point measurements. *Combust. Sci. Technol.* **2008**, *180*, 927–940.
26. Delichatsios, M.A. A phenomenological model for smoke-point and soot formation in laminar flames. *Combust. Sci. Technol.* **1994**, *100*, 283–298.
27. Walls, J.R.; Strickland-Constable, R.F. Oxidation of carbon between 1000 and 2000 °C. *Carbon* **1964**, *1*, 335–338.
28. Djilali, N.; Gartshore, I.; Salcudean, M. Calculation of convective heat transfer in recirculating turbulent flow using various near-wall turbulence models. *Numer. Heat Transf*. **1989**, *16*, 189–212.
29. Kanury, A.M. *Introduction to Combustion Phenomena*; Gordon: New York, NY, USA, 1984.
30. Lautenberger, C.; Fernandez-Pello, C. Generalized pyrolysis model for combustible solids. *Fire Saf. J*. **2009**, *44*, 819–839.
31. Consalvi, J.L.; Pizzo, Y.; Porterie, B. Numerical analysis of the heating process in upward flame spread over thick PMMA slabs. *Fire Saf. J*. **2008**, *43*, 351–362.
32. Himoto, K.; Tanaka, T. A burning model for charring materials and its application to the compartment fire development. *Fire Sci. Technol*. **2004**, *23*, 170–190.
33. Wu, P.K. Heat flux pipe in large-scale fire tests. In Proceedings of the Eighth International Symposium on Fire Safety Science, Beijing, China, 18–23 September 2005; pp. 1413–1424.
34. Lois, E.; Swithenbank, J. Fire Hazards in Oil Tank Arrays in a Wind. *Symp. Combust.* **1979**, *17*, 1087–1098.